140
2-12-80
DR. 705

DOE/JPL/954356-2

MASTER

SILICON-ON CERAMIC PROCESS

Silicon Sheet Growth and Device Development for the Large-Area Silicon Sheet and Cell Development Tasks of the Low-Cost Solar Array Project

Quarterly Report No. 12 for April 2—June 29, 1979

By
P. W. Chapman
J. D. Zook
J. D. Heaps
B. L. Grung
B. Koepke
S. B. Schuldt

July 31, 1979
Date Published

Work Performed Under Contract No. NAS-7-100-954356

Honeywell Corporate Material Sciences Center
Bloomington, Minnesota

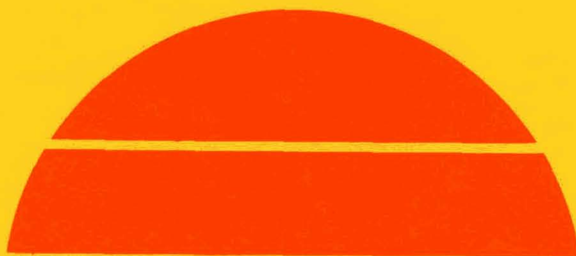

U.S. Department of Energy

DISTRIBUTION OF THIS DOCUMENT IS UNLIMITED

Solar Energy

DISCLAIMER

This report was prepared as an account of work sponsored by an agency of the United States Government. Neither the United States Government nor any agency Thereof, nor any of their employees, makes any warranty, express or implied, or assumes any legal liability or responsibility for the accuracy, completeness, or usefulness of any information, apparatus, product, or process disclosed, or represents that its use would not infringe privately owned rights. Reference herein to any specific commercial product, process, or service by trade name, trademark, manufacturer, or otherwise does not necessarily constitute or imply its endorsement, recommendation, or favoring by the United States Government or any agency thereof. The views and opinions of authors expressed herein do not necessarily state or reflect those of the United States Government or any agency thereof.

DISCLAIMER

Portions of this document may be illegible in electronic image products. Images are produced from the best available original document.

NOTICE

This report was prepared as an account of work sponsored by the United States Government. Neither the United States nor the United States Department of Energy, nor any of their employees, nor any of their contractors, subcontractors, or their employees, makes any warranty, express or implied, or assumes any legal liability or responsibility for the accuracy, completeness or usefulness of any information, apparatus, product or process disclosed, or represents that its use would not infringe privately owned rights.

This report has been reproduced directly from the best available copy.

Available from the National Technical Information Service, U. S. Department of Commerce, Springfield, Virginia 22161.

Price: Paper Copy $4.00
Microfiche $3.00

DOE/JPL/954356-2
Distribution Category UC-63b

DISCLAIMER

This book was prepared as an account of work sponsored by an agency of the United States Government. Neither the United States Government nor any agency thereof, nor any of their employees, makes any warranty, express or implied, or assumes any legal liability or responsibility for the accuracy, completeness, or usefulness of any information, apparatus, product, or process disclosed, or represents that its use would not infringe privately owned rights. Reference herein to any specific commercial product, process, or service by trade name, trademark, manufacturer, or otherwise, does not necessarily constitute or imply its endorsement, recommendation, or favoring by the United States Government or any agency thereof. The views and opinions of authors expressed herein do not necessarily state or reflect those of the United States Government or any agency thereof.

MASTER

SILICON-ON CERAMIC PROCESS

Silicon Sheet Growth and Device Development for the Large-Area Silicon Sheet and Cell Development Tasks of the Low-Cost Solar Array Project

Quarterly Report No. 12

by

P.W. Chapman
J.D. Zook, J.D. Heaps, B.L. Grung,
B. Koepke, and S.B. Schuldt

Period Covered: 4/2/79-6/29/79

Published: 31 July 1979

Honeywell Corporate Material Sciences Center
10701 Lyndale Ave. South
Bloomington, Minnesota 55420

The JPL Low-Cost Solar Array Project is sponsored by the U.S. Department of Energy and forms part of the Solar Photovoltaic Conversion Program to initiate a major effort toward the development of low-cost solar arrays. This work was performed for the Jet Propulsion Laboratory, California Institute of Technology, by agreement between NASA and DOE.

DISTRIBUTION OF THIS DOCUMENT IS UNLIMITED

THIS PAGE

WAS INTENTIONALLY

LEFT BLANK

TABLE OF CONTENTS

	Page
SUMMARY	1
INTRODUCTION	3
TECHNICAL DISCUSSION	5
Sheet Silicon Growth	5
Experimental Dip-Coater	5
Results	5
Dip-Coating Production	10
Continuous Coating Process	12
Cell Fabrication and Development	14
Optimum Base Doping Concentration	15
Effects of Growth Velocity on Cell Performance	16
Calculated Values of Series Resistance	26
Effects of Series Resistance	28
Material Evaluation	29
Loss in Short-Circuit Current Due to a Grain Boundary	34
Growth Modeling	40
Review of Symmetric Growth Model	41
Ribbon Thickness in Asymmetric Growth	43
Temperature Profile in the Solidification Region	44
Matching the Temperature Distribution to the Downstream Region	46
Two-Dimensional Verification	50
CONCLUSIONS AND RECOMMENDATIONS	53
Conclusions	53
Recommendations	54
PROJECTION OF FUTURE ACTIVITIES	55
NEW TECHNOLOGY	56
PROGRAM STATUS UPDATE	57
REFERENCES	60

LIST OF ILLUSTRATIONS

Figure		Page
1	Schematic Showing Different Gas Flow Pattern of Each Cooling Shoe	6
2	Photograph of Substrate Coated at 0.1 cm/sec with Gas Flowing Through Cooling Shoe Directed at Front Side of Substrate	7
3	Photograph of Substrate Coated at 0.15 cm/sec with Passive Graphite Afterheater in Place and Cooling Jets Directed at the Back Side of the Substrate.	9
4	SOC Sheet Silicon Showing Dip-Coated and SCIM-Coated Substrates	13
5	Silicon Meniscus with Tilted Substrate as Observed through the Viewing Port of the SCIM Coater	14
6	Current-Voltage Characteristics of a Recent 10-cm^2 SOC Solar Cell	15
7	Performance of Slotted SOC Cells as a Function of Base Doping Concentration, for Cells without AR Coating	24
8	Performance of Slotted SOC Cells as a Function of Base Doping Concentration, for Cells with AR Coating	25
9	Current-Voltage Characteristics of a Slotted SOC Cell Made from Material Grown at 0.08 cm/sec	26
10	Dark Characteristics of SOC Cell No. 108-4-102-1	30
11	Light Current-Voltage Characteristics for SOC Cell No. 180-4-102-1	31
12	Conversion Efficiency as a Function of Specific Series Resistance	31
13	LBIC Scans of a SCIM-Coated SOC Sample Taken by the Electrolyte Method	32
14	Diffusion Length, L_n, with Grains and Sheet Resistance, ρ_s, as Functions of the Dip Number for Dip Run 185	33
15	Geometry Used for Analysis of Grain Boundary Effects on Light Beam Response	35
16	Calculated LBIC Response at a Grain Boundary Having Infinite Surface Recombination Velocity.	38
17	Effective Grain Boundary Width, w, as a Function of αL	39
18	Silicon Ribbon Growth in (a) Symmetric and (b) Asymmetric Modes	40
19	Heat Fluxes from Solidification Region (Dashed) and into Downstream Region (Solid).	43

Figure		Page
20	Nonvertical Implementation of Asymmetric Growth	44
21	Linear Temperature Distribution in a Wedge-Shaped Solidification Region	45
22	Original (q_o) and Afterheater-Modified (q) Temperature Gradients for the Case v = 0.1 cm/sec, t = 0.04 cm	48
23	Linear Temperature Distribution to be Extended to $x = 1.2\,\ell$	49
24	Boundary Conditions for Numerical Integration of Equation (32)	50
25	Two-Dimensional Temperature Distribution in Silicon Ribbon Drawn Through the Heated Environment, $T_A(x)$ (dashed curve)	51
26	Two-Dimensional Temperature Distribution in Silicon Ribbon with No Heated Environment	52
27	Updated Program Plan	57
28	Updated Program Labor Summary	58
29	Updated Program Cost Summary	59

LIST OF TABLES

Table		Page
1	Coating Data for Run 439	8
2	Dip-Coating Production During Second Quarter 1979	11
3	Conversion Efficiencies and Other Characteristics of Recent Slotted-Substrate SOC Cells	17
4	Characteristics of Recent Slotted SOC Cells and Their Corresponding Single-Crystal Control Cells	19
5	Specific Series Resistance versus Base Doping Concentration and Thickness	28
6	Fitted Parameters for SOC Cell No. 180-4-102-1	29
7	Values for Silicon Parameters	42

SUMMARY

The objective of this research program is to investigate the technical and economic feasibility of producing solar-cell-quality sheet silicon. We plan to do this by coating one surface of carbonized ceramic substrates with a thin layer of large-grain polycrystalline silicon from the melt.

During the quarter, we demonstrated signigicant progress in several areas:

- We succeeded in fabricating a 10-cm^2 cell having 9.9 percent conversion efficiency (AM1, AR).
- The Honeywell-sponsored SCIM coating development succeeded in producing a 225-cm^2 layer of sheet silicon (18 inches x 2 inches).
- 100μm-thick coatings at pull speed of 0.15 cm/sec were obtained, although approximately 50 percent of the layer exhibited dendritic growth.

Other results and accomplishments during the quarter can be summarized as follows:

- Initial indications are that the introduction of convective cooling at the liquid-solid interface does provide thicker, smoother coatings for a given pull rate.
- The silicon carbide formation problem appearing in the production dipcoater was due to a leak in the argon line and has been resolved.
- Unidirectional solidification occurred in layers pulled at 0.2 cm/sec in the production dipcoater, even though these layers were very thin (~6 μm).
- Vitreous carbon-coated substrates obtained from Tylan Corp. were dipped and shipped to JPL for evaluation.
- Tilting of the SCIM coater produced meniscus stability, and the long-awaited "good" layers were produced by the SCIM coater.
- A total of 86 silicon-on-ceramic (SOC) solar cells were fabricated, 52 of which were AR coated. Fourteen of these cells had >9 percent conversion efficiency.

- The standard coating parameters for good cell performance are: ND = 1×10^{16} boron atoms/cc and a pull speed of 0.07 cm/sec.
- A 9.1 percent conversion efficiency, 4-cm^2 total area cell (AR, AM1) was fabricated on SOC material 120 μm thick pulled from the dipcoater at 0.08 cm/sec.
- Calculated values of series resistance in SOC cells indicate little effect on cell performance as the silicon layer gets thinner.
- An LBIC scan of SCIM-coated material indicates a diffusion length of L_n = 34 ± 3 μm.
- A model has been derived for loss in short-circuit current due to grain boundaries. The model gives reasonable values compared with LBIC data.
- Mathematical modeling of unsupported symmetric and asymmetric growth was continued.

INTRODUCTION

This research program began on 21 October 1975. Its purpose is to investigate the technical and economic feasibility of producing solar-cell-quality sheet silicon by coating inexpensive ceramic substrates with a thin layer of polycrystalline silicon. The coating methods to be developed are directed toward a minimum-cost process for producing solar cells with a terrestrial conversion efficiency of 11 percent or greater.

By applying a graphite coating to one face of a ceramic substrate, molten silicon can be caused to wet only that graphite-coated face and produce uniform thin layers of large-grain polycrystalline silicon; thus, only a minimal quantity of silicon is consumed. A dip-coating method for putting silicon on ceramic (SOC) has been shown to produce solar-cell-quality sheet silicon. This method and a continuous coating process also being investigated have excellent scale-up potential which offers an outstanding, cost-effective way to manufacture large-area solar cells. The dip-coating investigation has shown that, as the substrate is pulled from the molten silicon, crystallization continues to occur from previously grown silicon. Therefore, as the substrate length is increased (as would by the case in a scaled-up process), the expectancy for larger crystallites increases.

A variety of ceramic materials have been dip-coated with silicon. The investigation has shown that mullite substrates containing an excess of SiO_2 best match the thermal expansion coefficient of silicon and hence produce the best SOC layers. With such substrates, smooth and uniform silicon layers 25 cm^2 in area have been achieved with single-crystal grains as large as 4 mm in width and several cm in length. Crystal length is limited by the length of the substrate. The thickness of the coating and the size of the crystalline grains are controlled by the temperature of the melt and the rate at which the substrate is withdrawn from the melt.

The solar-cell potential of this SOC sheet silicon is promising. To date, solar cells with areas from 1 to 10 cm^2 have been fabricated from material with an as-grown surface. Conversion efficiencies of about 10 percent with antireflection (AR) coating have been achieved. Such cells typically have open-circuit voltages and short-circuit current densities of 0.55V and 23 mA/cm^2, respectively.

Ths SOC solar cell is unique in that its total area is limited only by device design considerations. Because it is on an insulating substrate, special consideration must be given to electrical contact to the base region. One method which offers considerable

promise is to place small slots in the substrate perpendicular to the crystalline growth direction and contact the base region by metallizing the silicon that is exposed through the slots on the back side of the substrate. Smooth, continuous coatings have been obtained on substrates which were slotted in the green state prior to high-temperature firing. The best slotted-cell results to date indicate a 10.1 percent conversion efficiency (AR-coated) on a 4-cm^2 (total area) cell.

Development efforts are continuing in such areas as improvement in growth rate, reduction of progressive melt contamination, and optimization of electrical contacts to the base layer of the cell. The investigation has shown that mullite substrates, to a limited extent, dissolve in molten silicon. The impurities from the substrate are believed to adversely affect solar-cell conversion efficiency. A method for reducing substrate dissolution is to reduce the contact area the substrate makes with the silicon melt. Therefore, a silicon coating facility, referred to as SCIM or Silicon Coating by an Inverted Meniscus, has been constructed which is designed to coat large (10 cm x 100 cm) substrates in a continuous manner. It is expected that this facility will not only improve the growth rate, but also minimize the silicon melt contact with the substrate. This should reduce the rate at which the melt becomes contaminated. The facility will also permit a study of possible continued grain growth by accommodating the use of longer substrates. It should also reveal problems that are likely to be encountered in a scale-up process. This machine has succeeded in demonstrating coatings exhibiting unidirectional solidification (desirable and occurring in dip coating) on substrates 18 inches long and 2 inches wide. Material characteristics indicate this material is similar in structure and purity to material obtained from our dip-coating facilities.

TECHNICAL DISCUSSION

SHEET SILICON GROWTH (J. D. Zook, J. D. Heaps, B. Koepke, L. D. Nelson, D. J. Sauve, O. Harris, and H. Burke)

Experimental Dip-Coater (B. Koepke, D. Zook, D. Sauve)

During the past quarter, a series of runs were made with the experimental dip coater in an effort to improve the throughput of the coating process. Our goal this year is to produce smooth, 100 μm-thick nondendritic coatings at a solidification rate of 0.3 cm/sec. Most of the runs were made with cooling shoes positioned near the liquid-solid interface. The shoes were water-cooled and had argon gas flowing through them onto the front and/or back sides of the substrate. Figure 1 shows the geometry of the gas jets in each shoe. In one case (shoe I), the gas flows out parallel to the long direction of the shoe and impinges on the substrate at an angle as shown in the Figure 1. In the other case (shoe II), the gas flow is perpendicular to the substrate surface. This difference might be of some significance in view of the high meniscus below the liquid solid interface. Shoe I can be used to cool the back side of the substrate below the liquid-solid interface as shown in Figure 1. As noted in Quarterly Report No. 11, both cooling shoes can be moved in the x and y directions without having to open the system during a run, thereby giving considerable flexibility to the cooling supplied near the liquid-solid interface.

Results

Results will be discussed with respect to each run. A run refers to the substrates dipped during a single day. Typically, 10 to 12 substrates are coated during a run.

Run 429 (All Unslotted Substrates) -- The pull rate was fixed at 0.2 cm/sec. With no cooling, the coating was 75 percent dendritic and the smooth sections were 10 to 20 μm thick. With front and back shoes in place, the coatings were still mostly dendritic. The thickness of the smooth portions increased from 10 to 25 μm as the gas flow increased.

Run 430 (All Unslotted Substrates) -- Substrates were mostly coated at 0.1 cm/sec with only shoe II (see Figure 1) in place. The coatings were about 100 μm thick and varied in thickness across the width of the substrate. The thicker regions corresponded to areas that were closest to the gas jets. When the pull rate was increased to 0.2 cm/sec, the coatings were smooth and the thickness decreased to 25 μm but still had the vertical "stripes" corresponding to where each gas jet impinged on the substrate.

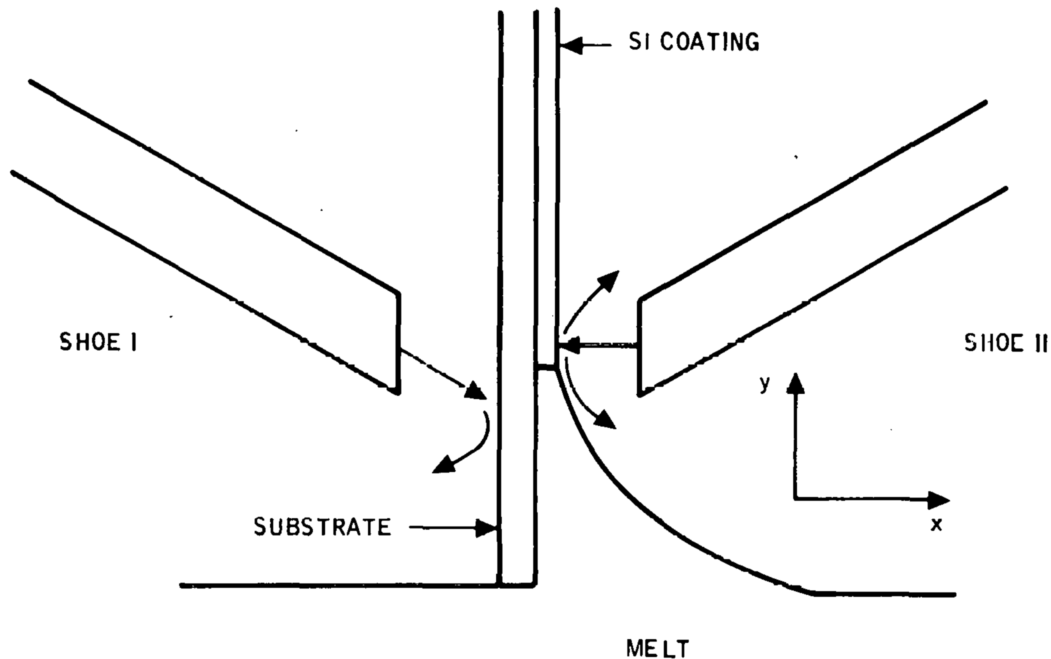

Figure 1. Schematic Showing Different Gas Flow Pattern of Each Cooling Shoe. The arrows show the expected flow directions.

An interesting substrate dipped during this run deserves mention. The pull rate was 0.1 cm/sec and cooling shoe I only was used. The gas was turned on after one-third of the substrate was coated. Before the gas was turned on, a smooth, 50 μm-thick coating formed. After the gas was turned on, a coating (with vertical "stripes") formed that was partly dendritic and 125 μm thick in the thickest regions. This substrate (430-6) is shown in Figure 2. This was the thickest coating obtained at the time at 0.1 cm/sec.

Run 431 (All Unslotted Substrates) -- During this run, cooling shoe II only was used and the pull rate was steadily increased from 0.05 to 0.2 cm/sec. The coatings were typically 20 percent dendritic and the smooth regions had nominal thicknesses of 100 μm at 0.1 cm/sec, 50 μm at 0.125 cm/sec, and 15 μm at 0.15 to 0.2 cm/sec.

In each dip, the gas was turned on after one-third of the substrate had been coated, and the speed was increased only after the gas was on. In every case, when the gas was turned on at 0.05 cm/sec, the smooth coating remained smooth and increased in thickness. The thickness then decreased as the pull speed increased. We conclude from these runs that gas cooling can definitely increase the thickness of the coating.

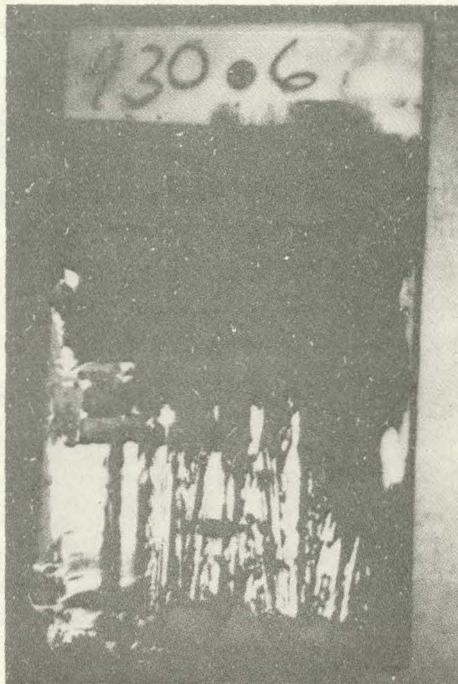

Figure 2. Photograph of Substrate Coated at 0.1 cm/sec with Gas Flowing Through Cooling Shoe Directed at Front Side of Substrate. The vertical stripes correspond to where the gas jets impinge on the substrate. The gas was turned on after one-third of the substrate had been coated.

Run 432 (Slotted Substrates) -- During this run, slotted substrates were used to more closely match the cooling conditions used on material fabricated into cells. At pull rates of 0.1 cm/sec with shoe II on the front side, smooth coatings turned partially dendritic when the gas was turned on and the smooth regions of the coatings never exceeded 75 μm in thickness.

Run 433 (Slotted Substrates) -- In this run, only shoe II was used on the back side of the substrate. In most cases, the slots did not completely coat at any of the gas flow rates used.

Run 434 (Unslotted Substrates) -- Severe cracking problems were encountered and only thin (25 to 50 μm) coatings were produced. The origin of the cracking is not understood.

Run 435 (Slotted and Unslotted Substrates) -- Shoe II was directed at the back side of the substrate. The pull rate was 0.1 cm/sec and most of the coatings were at least 50 percent dendritic. The thickest smooth portion of a coating that was produced was only 100 μm.

Run 436 (Slotted Substrates) -- This was a demonstration run for the Chief Executive Officer of Honeywell. All coating was carried out at 0.05 cm/sec with no cooling. The coatings were all smooth and had thicknesses ranging from 200 to 300 μm.

Run 437 (Slotted Substrates) -- During this run, a passive "afterheater" was installed to alleviate the substrate cracking problem. The heater consisted of a mullite tube suspended over the melt. It was supposed that the tube, heated by radiation from the crucible heater and melt surface, would both preheat the substrate and decrease the temperature gradient above the melt to minimize cracking during coating. With shoe I directed at the front of the substrates, the substrates shattered when the gas was turned on.

Run 438 (Slotted Substrates) -- In this run, a passive "afterheater" made of graphite was used. The graphite tube was set directly on the heat shield surrounding the heater to allow heating of the afterheater by both conduction and radiation. With shoe I directed at the back side of the substrate, runs were made at a pull rate of 0.1 cm/sec at a number of gas flows and the substrates did not crack; on the other hand, the coating thickness never exceeded 75 μm.

Run 439 (Slotted Substrates) -- In this run, the passive graphite afterheater was again used with shoe I directed at the back of the substrate. Cracking was not observed and the best results to date were observed. These results are listed in Table 1.

Table 1. Coating Data for Run 439

Substrate	Pull Rate (cm/sec)	Gas Cooling (No. of turns of gas valve)	Coating Thickness (μm)	Area of Dendrites (%)	Coverage (%)
1 CKH	0.05	0	500	0	100
2 CKH	0.1	0	100	80	100
3 CKH	0.2	0	*	100	100
4 CKH	0.1	4	25	40	50
5 CKH	0.15	4	40 to 50	30	30
6 CKH	0.15	8	80	50	2 open slots
7 CKH	0.15	12	50 to 125	50	4 open slots
8 CKH	0.15	16	40 to 60	50	3 open slots

*No smooth regions to measure thickness.

Substrates No. 7 and 8 CKH warrant discussion. First, the 125 μm-thick regions on the smooth portions of No. 7 CKH (shown in Figure 3) are the thickest smooth coatings produced to date. Second, both substrates exhibited horizontal variations in thickness corresponding to the positions of the gas jets in the cooling shoe. Finally, it is interesting to note that the thickness decreased as the gas flow rate increased, implying that heat transfer (or other factors) may be optimum at intermediate flow rates.

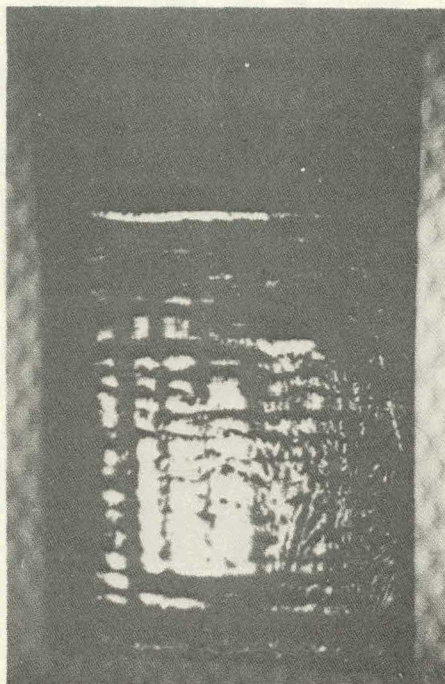

Figure 3. Photograph of Substrate Coated at 0.15 cm/sec with Passive Graphite Afterheater in Place and Cooling Jets Directed at the Back Side of the Substrate. The vertical stripes correspond to where the cooling jets impinged on the substrate. The thicker regions are 125 μm thick.

Run 440 (Slotted Substrates) -- There was another demonstration run and cooling shoes were not used.

This work is continuing. It is realized that an active afterheater will be necessary to prevent fracture of the substrates. A graphite resistance heater designed by D. Heaps is currently being installed in the system and will shortly be in operation. The heater will be powered by unregulated a-c current through a stepdown transformer. If the afterheater is successful, a series of runs will be made in which the gas pressure through the shoes will be systematically varied. It is premature to consider optimizing the number or position of the shoes with respect to the liquid-solid interface. The melt temperature, to date, has been fixed at that temperature yielding thick, smooth coatings at 0.05 cm/sec with no cooling. In the next phase of this study, the melt temperature will be varied.

Dip-Coating Production (D. Zook and V. Harris)

During the quarter, the production dip-coating system produced SOC material under a variety of conditions as well as "standard" material for cell fabrication studies. The run numbers and relevant data are summarized in Table 2.

The six runs listed first in Table 2 were done under standard conditions of doping and growth speed. Various system procedures were changed, however, in an attempt to prevent the formation of SiC particles on the melt surface. For example, run number 426 was a production-type run performed in the experimental dip coater to see if SiC appeared in that system after a large number of dips. For run number 170, the SiC problem was resolved. It was due to a leak in the packing seal of a valve in the argon line. The valve was seating properly so that there was no leak at zero or low flow rates, but only at the normal flow rate during dipping.

The mechanism of SiC formation is very likely that discussed in the recent article by Schmid, et al:[1]

$$2Si + CO \rightarrow SiC + SiO$$

This reaction will proceed if the pressure of CO is 7 percent of the pressure of SiO or greater. The pressure of SiO is probably a few torr in the vicinity of the melt due to dissolution of the silica crucible. The CO was formed from the O_2 leak by reaction with the graphite heaters. From Schmid's argument, some SiC will always form, but we do not see it on the melt, except in the case of an air leak. Normally, it is presumably carried away by the substrate, trapped at the silicon-carbon interface, and should therefore not be a problem even in 24-hour operation of an SOC coating process.

Runs 179 through 185 were designed to cover a wide range of dopings and thicknesses. By varying the speed from 0.06 to 0.08 cm/sec, the thickness varies from 240 μm to 100 μm. These are not the maximum thicknesses at those speeds, but are typical when the melt temperature is adjusted to completely avoid dendritic growth and therefore give maximum yield.

Run 186 was dedicated to evaluation of slotted substrates coated with vitreous carbon by Tylan, using a low-cost process that they developed under JPL funding. Unfortunately, there was some carbon on the inner edges of the slots, and we have always observed that this perturbs the growth. In retrospect, if those substrates had been coated at very slow speeds, they might have yielded good layers. The substrates have all been shipped to JPL for evaluation.

Table 2. Dip-Coating Production During Second Quarter 1979

Run Number	Dopant Level (10^{16} boron/cm^3)	Growth Speeds (cm/sec)	Number Dipped	Comments
174	2.3	0.06	13	"Standard" conditions, good yield.
426	2.3	0.06	17	No SiC formation in experimental system.
175	2.3	0.06	17	SiC after No. 10.
176	2.3	0.06	12	SiC after No. 8.
177	2.3	0.06	10	SiC after No. 8.
178	2.3	0.06	15	SiC after No. 7. New heater shield leak corrected; no SiC formation.
179	0.47	0.06, 0.07, 0.08	15	
180	0.93	0.06, 0.07, 0.08	10	
181	0.93	0.06, 0.07, 0.08	27	
182	4.7	0.06, 0.07, 0.08	14	
183	1.4	0.06, 0.07, 0.08	12	
184	0.23	0.06, 0.07, 0.08	21	
185	0.23	0.06, 0.07, 0.08	25	
186	2.3	0.06		Vitreous carbon (Vitregraph).
187	2.3	0.06	11	5 + soak + 5.
188	0.23	0.06	16	Dag experiment, poor coatings.
189	2.3	0.06 to 0.20	9	For evaluation of very thin material.
190	0.93	0.07 to 0.20	16	(189 and 190:) For evaluation of very thin material.
191	0.93	0.07 to 0.10	32	Dag experiment, good coatings.
192	0.93	0.07	12	New "standard" conditions.
193	0.93	0.07	15	Type "N" and "O" substrates.

Run 187 was designed to compare the effect of a long soak time with the results of long run (181 and 185). Five substrates were dipped in the normal way, and then one substrate was soaked for 1 hour, and five more substrates were dipped. Experiments of this type should show whether the reaction between the silicon and the mullite passivates the mullite to prevent diffusion of impurities.

Run 188 was designed to see if carbon coatings can prevent melt contamination. Dag carbon coatings were used on both sides of unslotted substrates. Unfortunately, the carbon peeled off and the experiment had to be repeated. Run 191 was a repetition, except that the speeds were varied.

Runs 189 and 190 were done at high dip speeds with unslotted substrates in order to obtain very thin material for evaluation. It is interesting that coatings at 0.1 cm/sec produced material 56 ± 10 μm thick with large grain size. Grain boundary counting will be used to determine whether the grain size varies statistically as a function of thickness (growth speed), but qualitatively, there is little difference in the structure or grain size. At 0.15 cm/sec and 0.20 cm/sec, there is a definite change in appearance; the surface is definitely rougher. However, there was still good evidence of unidirectional solidification and reasonably large grain size, even at speeds of 0.2 cm/sec, which gives a thickness of 6 μm in the present production system.

Continuous Coating Process (D. Heaps, L. D. Nelson, H. Burne) [Honeywell funded]

During the past quarter, the continuous (SCIM) coater was extensively modified. The two most significant changes that were made were:

1) A motor-driven mechanism was added which permitted tilting the coater at various angles up to 30 degrees above horizontal.

2) New crucible and trough heaters were added which provided superior thermal independence and temperature uniformity than was previously attainable.

To date, six successful coating runs have been made with the coater tilted at a small angle. Smooth, shiny silicon layers were coated on 5 cm x 55 cm x 0.1 cm mullite substrates (K-modification) at a coating velocity of 0.06 cm/sec. The best one of these silicon coated substrates is shown in Figure 4. As shown, this substrate was for the most part uniformly coated over an area of 225 cm^2 and had a nominal thickness of ~ 100 μm. The layer consisted of large columnar silicon grains virtually identical to those achieved by dip coating under similar growth parameters. Preliminary minority carrier diffusion length (L_n) measurements made on one of these coatings indicates an

L_n value which is also similar to dip coated silicon. Due to a small, but still existing thermal gradient along the trough, the layers varied in thickness from one side of the substrate to the other side.

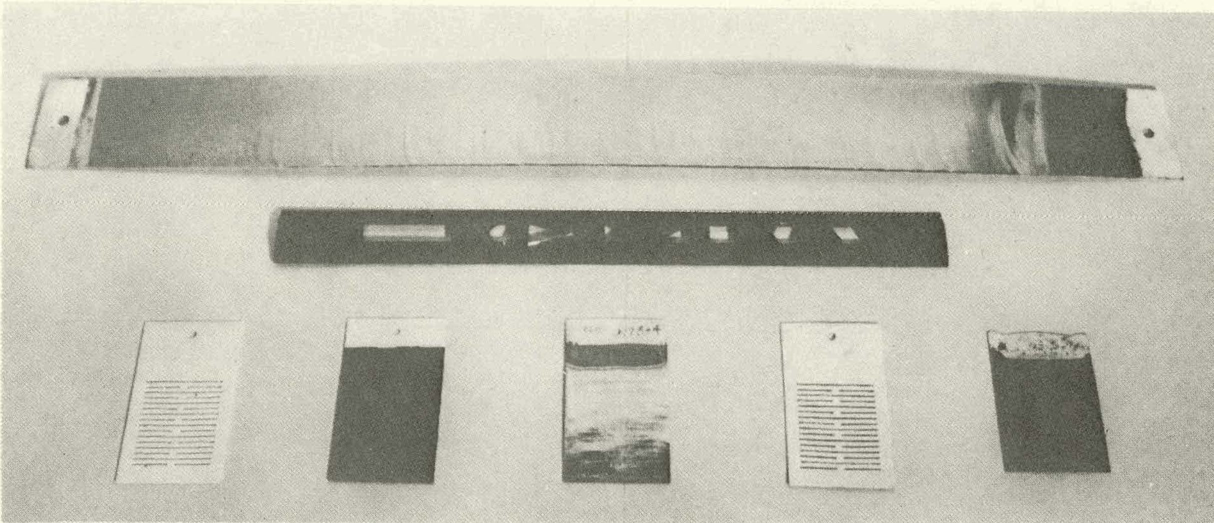

Figure 4. SOC Sheet Silicon Showing Dip-Coated and SCIM-Coated Substrates

The above results are of considerable significance, since they demonstrate that by passing the substrate at an angle over the silicon-filled trough, the long sought after meniscus stability necessary to SCIM coating has been achieved. The above results also clearly demonstrated that the overall sheet silicon area of any single coating is limited only by the physical dimensions of the substrate. It was made clear, however, that temperature uniformity along the trough is of utmost importance. The above results further demonstrate that because of the similar nature of the SCIM-coated layers, all of our past development efforts on dip-coated layers should be applicable to the SCIM-coated layers as well.

As shown by Fig 5, the liquid-solid interface appears to occur along a straight line ~8 mm downstream of the trough. This observation is based on the fact that the temperature of the back surface of the substrate is elevated where the substrate is in contact with molten silicon. The location of this interface with respect to the melt is not unlike that of dip

coating which produces a condition which is conducive to meniscus stability. To date, no effort has been made to optimize the coating angle θ.

During the coming quarter, an effort will be made to correct the thermal gradient along the trough, making it possible to silicon coat wider substrates. We will also investigate effects that such coating parameters as coating angle, coating speed, substrate temperature, and meniscus temperature have on layer quality. Large-area slotted substrates will be ordered, and, time permitting, these substrates will also be coated.

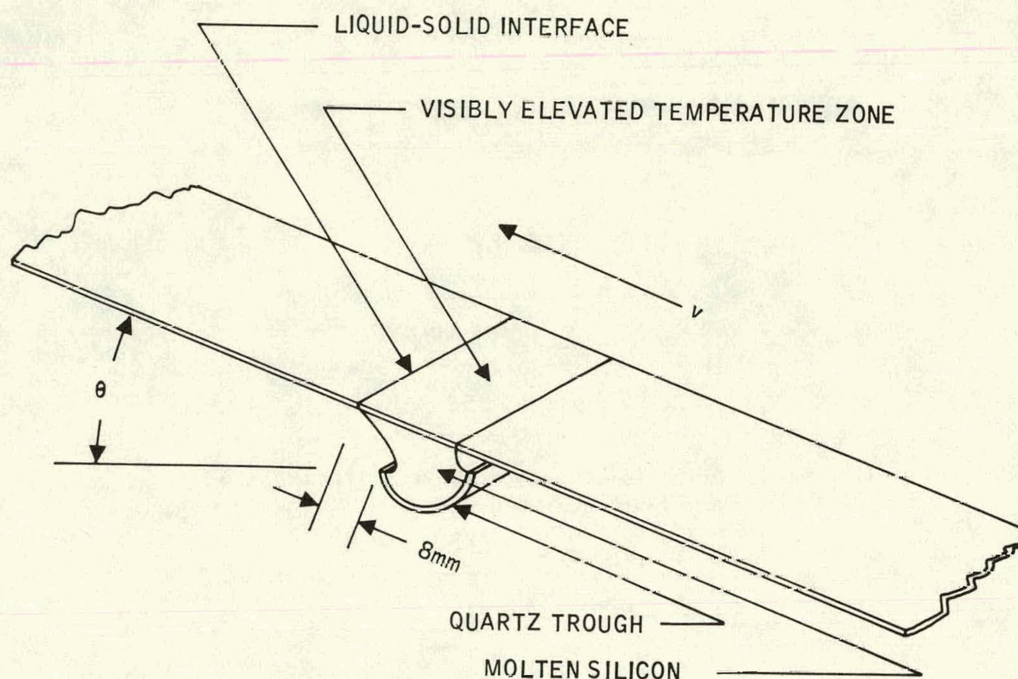

Figure 5. Silicon Meniscus with Tilted Substrate as Observed through the Viewing Port of the SCIM Coater

CELL FABRICATION AND DEVELOPMENT
(B. Grung, T. Heisler, and S. Znameroski)

Presently, the best 10-cm^2 SOC cell has a conversion efficiency of 9.91 percent (AM1, AR). The current-voltage characteristics of this cell are given in Fig 6 The cell has an open-circuit voltage, V_{oc}, of 0.56 V, a fill factor (FF) of 0.71, a short-circuit current density, J_{sc}, of 24.9 mA/cm^2, and a metallization coverage of 8 percent. The latter two values give an active-area J_{sc} of 26.9 mA/cm^2, which indicates good material quality. An ELH lamp was used for all measurements and the reference cell (No. TSS-38) was calibrated by JPL.

During this quarter, a total of 86 SOC cells were fabricated and 52 of these were AR coated. The primary characteristics of all cells are listed in Tables 3 and 4, along with the characteristics of corresponding single-crystal control cells. Of the 52 AR-coated cells, 14 had conversion efficiencies in the range from 9 to 10 percent.

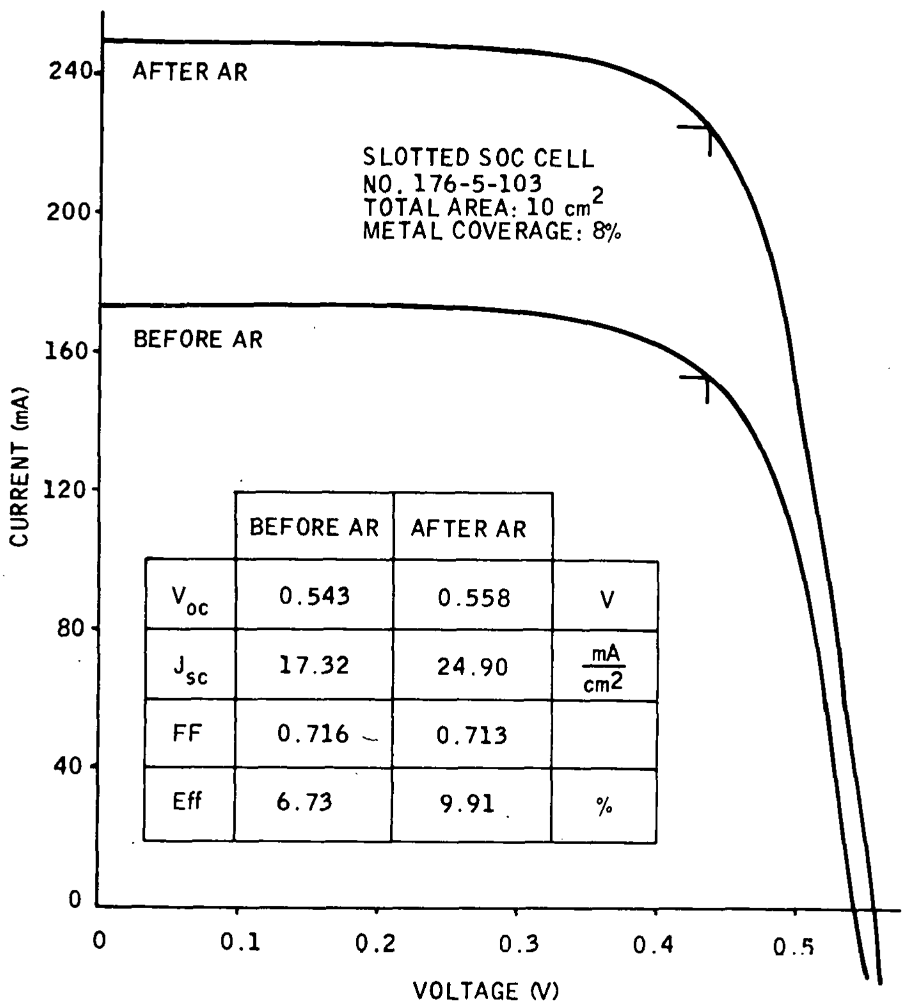

	BEFORE AR	AFTER AR	
V_{oc}	0.543	0.558	V
J_{sc}	17.32	24.90	mA/cm2
FF	0.716	0.713	
Eff	6.73	9.91	%

Figure 6. Current-Voltage Characteristics of a Recent 10-cm^2 SOC Solar Cell

Optimum Base Doping Concentration

Our main objective during this quarter was to determine the optimum base doping concentration for SOC cells and to investigate the effects of growth speed on cell performance. The cells in Table 3 and 4 are listed first by base doping concentration then by growth speed, and finally by cell number. The base doping conventrations are 2.3×10^{15}, 4.7×10^{15}, 9.3×10^{15}, 2.3×10^{16}, and 4.7×10^{16}/cm. The growth velocities are 0.00,

0.07, and 0.08 cm/sec. For the 1978 baseline cells, the standard base doping concentration was $2.3 \times 10^{16}/cm^3$ and the standard growth speed was 0.06 cm/sec. Because of the results given here, the present standard base doping concentration is $10^{16}/cm^3$ and the present standard growth speed is 0.07 cm/sec.

For each of the 86 SOC cells, Table 3 lists the cell number, base doping concentration, growth speed, specific series resistance, base sheet resistance, and conversion efficiencies before and after AR coating. Each cell is identified by the same item number in Tables 3 and 4. For each cell, Table 4 lists the measured values of I_{sc}, V_{oc}, FF, J_{sc}, and η. for conditions before and after AR coating. Some of the data presented in Tables 3 and 4 are summarized in Figures 7 and 8, where the former is for conditions before AR coating and the latter is for conditions after. Since both figure are very similar, we will now consider only the AR-coated results.

Figure 8 shows how the base doping concentration affects the performance of slotted SOC cells. Figure 8(a) shows that the open-circuit voltage, V_{OC}, increases as the base doping concentration N_{BG} increases from 10^{15} to $10^{16}/cm^3$ and is relatively constant for larger values. For a given value of N_{BG}, the center of the vertical line indicates the average value of V_{OC} and the length of the line is 2σ. where σ is the standard deviation. Thus, for a base doping concentration of $2.3 \times 10^{16}/cm^3$ (which was the standard concentration for the 1978 baseline cells), the average value was 0.536 V, with a standard deviation of 0.005 V. The solid line indicates approximately how the average value of V_{OC} should vary as a function of N_{BG}, based on the data measured at the six different values of N_{BG}. Figure 8(b) shows that the fill factor, FF, is nearly independent of N_{BG}, as expected. Figure 8(c) shows that, as N_{BG} increases, the total-area short-circuit current density first increases to a maximum value of 24.6 mA/cm^2 and then decreases. The maximum value occurs for a H_{BG} value of $10^{16}/cm^3$, which is the present standard base doping concentration. Figure 8(d) shows that the conversion efficiency, η. also has a maximum value for the same value of N_{BG}.

Effects of Growth Velocity on Cell Performance

Figure 9 shows the current-voltage characteristics of cell number 179-9-102, which was fabricated from SOC material grown at velocity of 0.08 cm/sec. As indicated, the cell has a total-area (4 cm^2) conversion efficiency of 9.08 percent (AM1, AR) and a specific series resistance of 1.0 Ω-cm^2. These two performance values are consistent with the typical values measured for the 1978 baseline cells, indicating that the production dip-coating system can produce good quality SOC material at a growth speed of 0.08 cm/sec. At this speed the silicon thickness is about 120 μm.

Table 3. Conversion Efficiencies and Other Characteristics of Recent Slotted-Substrate SOC Cells

item	Cell Number	P-type Doping (atoms/cc)	Dip Speed (cm/sec)	RA Product (ohms-sq cm)	Base Sheet Resistance	Total Area Conversion Efficiencies Before AR (%)	Total Area Conversion Efficiencies After AR (%)
1	182 - 8-101	4.7e+016	0.08	1.5	49	5.35	
2	182 - 8-202	4.7e+016	0.08	1.0	49	5.88	
3	182 -11-101	4.7e+016	0.07	1.4	31	5.37	7.89
4	182 -11-202	4.7e+016	0.07	1.0	31	5.52	7.67
5	182 -10-101	4.7e+016	0.06	1.1	21	6.05	8.54
6	182 -10-202	4.7e+016	0.06	0.8	21	5.34	8.16
7	178 -14-102	2.3e+016	0.07	2.0	50	4.49	6.54
8	178 -14-201	2.3e+016	0.07	1.4	50	5.06	7.43
9	165 - 1-101	2.3e+016	0.06		107	5.42	7.85
10	165 - 1-202	2.3e+016	0.06		107	5.51	8.06
11	165 -14-103	2.3e+016	0.06		43	5.42	8.16
12	166 - 6-101	2.3e+016	0.06	0.7	73	4.11	
13	166 - 6-202	2.3e+016	0.06		73	6.99	9.80
14	166 -10-101	2.3e+016	0.06		63	6.10	8.73
15	166 -10-202	2.3e+016	0.06		63	6.63	9.35
16	166 -15-101	2.3e+016	0.06	0.7	43	4.89	
17	166 -15-202	2.3e+016	0.06	1.1	43	6.34	8.93
18	167 - 5-102	2.3e+016	0.06	0.8	118	5.01	
19	167 - 5-201	2.3e+016	0.06	1.2	118	4.63	
20	167 - 5-302	2.3e+016	0.06	1.0	118	6.06	
21	167 -10-101	2.3e+016	0.06		75	5.99	8.25
22	167 -10-202	2.3e+016	0.06		75	6.12	8.45
23	167 -12-102	2.3e+016	0.06	0.8	94	6.69	
24	167 -13-102	2.3e+016	0.06	1.0	88	4.78	
25	168 - 8-101	2.3e+016	0.06		46	6.50	9.21
26	168 - 8-202	2.3e+016	0.06		46	5.20	7.49
27	168 - 9-102	2.3e+016	0.06	0.7	51	7.06	9.57
28	168 -11-102	2.3e+016	0.06	0.9	80	5.56	
29	168 -11-201	2.3e+016	0.06	1.3	80	5.76	
30	168 -12-101	2.3e+016	0.06		65	6.36	9.14
31	168 -12-202	2.3e+016	0.06	0.8	65	5.43	7.88
32	169 - 2-103	2.3e+016	0.06	1.6	63	6.42	
33	169 - 3-103	2.3e+016	0.06	0.8	54	6.67	9.75
34	169 - 5-101	2.3e+016	0.06	1.2	73	5.56	
35	169 - 5-202	2.3e+016	0.06	1.1	73	6.14	
36	169 - 6-102	2.3e+016	0.06	0.7	50	6.25	8.80
37	169 - 6-201	2.3e+016	0.06	1.1	50	6.14	8.82
38	170 - 1-102	2.3e+016	0.06	1.0	103	6.43	
39	170 - 8-202	2.3e+016	0.06	0.8	36	6.69	9.36
40	170 - 9-103	2.3e+016	0.06	0.9	58	6.27	
41	171 -13-103	2.3e+016	0.06	1.2	61	6.32	
42	175 - 4-103	2.3e+016	0.06	1.6	38	6.03	8.84
43	175 - 6-102	2.3e+016	0.06	1.1	41	7.15	
44	175 - 6-201	2.3e+016	0.06	1.4	41	6.18	
45	175 - 8-101	2.3e+016	0.06	1.0	55	6.66	
46	175 - 8-202	2.3e+016	0.06	0.7	55	3.91	
47	175 -12-101	2.3e+016	0.06	0.9	73	6.91	
48	175 -12-202	2.3e+016	0.06	0.6	73	5.67	

Table 3. Conversion Efficiencies and Other Characteristics of Recent Slotted-Substrate SOC Cells (Concluded)

item	Cell Number	P-type Doping (atoms/cc)	Dip Speed (cm/sec)	RA Product (ohms-sq cm)	Base Sheet Resistance	Total Area Conversion Efficiencies Before AR (%)	After AR (%)
49	175 -13-103	2.3e+016	0.06	0.9	32	5.82	
50	176 - 3-102	2.3e+016	0.06	0.7	51	7.26	
51	176 - 3-201	2.3e+016	0.06	0.9	51	6.09	
52	176 - 5-103	2.3e+016	0.06	1.2	54	6.73	9.91
53	176 - 7-103	2.3e+016	0.06	1.0	52	5.86	
54	178 -13-102	2.3e+016	0.06	0.8	46	5.48	
55	178 -13-201	2.3e+016	0.06	0.7	46	5.30	
56	426 - 3-101	2.3e+016	0.06	1.1	54	5.44	
57	426 - 3-202	2.3e+016	0.06	0.5	54	4.69	
58	426 - 4-103	2.3e+016	0.06	0.9	67	6.48	
59	183 - 6-102	1.4e+016	0.08	2.3	114	5.58	
60	183 - 6-201	1.4e+016	0.08	8.0	114	5.36	
61	183 - 5-102	1.4e+016	0.07	1.6	96	6.89	9.33
62	183 - 5-201	1.4e+016	0.07	3.7	96	6.79	9.24
63	183 - 7-102	1.4e+016	0.06	2.1	68	6.87	9.58
64	183 - 7-201	1.4e+016	0.06	2.3	68	6.41	8.90
65	180 - 6-201	9.3e+015	0.08	2.3	151	5.97	8.23
66	180 - 5-101	9.3e+015	0.07	5.2	137	6.10	8.06
67	180 - 5-202	9.3e+015	0.07	6.1	137	6.45	8.81
68	180 - 4-102	9.3e+015	0.06	2.2	98	7.09	9.53
69	180 - 4-201	9.3e+015	0.06	3.7	98	6.24	8.42
70	179 - 9-102	4.7e+015	0.08	1.0	160	6.50	9.08
71	179 - 9-201	4.7e+015	0.08	1.5	160	6.35	8.93
72	179 -15-102	4.7e+015	0.08	7.6	170	4.37	6.24
73	179 - 4-102	4.7e+015	0.07	1.6	291	6.63	8.58
74	179 - 4-201	4.7e+015	0.07	1.3	291	6.78	9.55
75	179 -14-102	4.7e+015	0.07	2.3	156	5.77	7.40
76	179 -14-201	4.7e+015	0.07	7.1	156	5.87	7.85
77	179 - 3-102	4.7e+015	0.06	1.7	303	6.72	8.96
78	179 - 3-201	4.7e+015	0.06	1.7	303	6.70	8.88
79	179 -13-102	4.7e+015	0.06	5.3	172	6.10	8.14
80	179 -13-201	4.7e+015	0.06	5.3	172	6.39	8.60
81	184 -12-102	2.3e+015	0.08		263	5.99	7.04
82	184 -12-201	2.3e+015	0.08	2.1	263	5.36	7.43
83	184 - 8-101	2.3e+015	0.07	2.0	355	5.21	7.32
84	184 - 8-202	2.3e+015	0.07	1.8	355	5.52	8.00
85	184 -10-102	2.3e+015	0.06	4.9	298	4.08	4.95
86	184 -10-201	2.3e+015	0.06	3.3	290	4.99	6.26

Table 4. Characteristics of Recent Slotted SOC Cells and Their Corresponding Single-Crystal Control Cells

item	Cell Number	Isc (mA)	Voc (V)	Fill Factor	Total-Area Jsc (mA/sqcm)	Total-Area Eff. (%)	
1	182 - 8-101-0	63.90	0.531	0.643	15.66	5.35	
2	182 - 8-202-0	63.30	0.537	0.706	15.52	5.88	
3	182 -11-101-0	65.10	0.528	0.637	15.96	5.37	
3	182 -11-101-1	91.50	0.541	0.650	22.43	7.89	(AR)
4	182 -11-202-0	62.50	0.532	0.677	15.32	5.52	
4	182 -11-202-1	87.10	0.545	0.659	21.35	7.67	(AR)
5	182 -10-101-0	63.10	0.540	0.724	15.47	6.05	
5	182 -10-101-1	88.20	0.554	0.713	21.62	8.54	(AR)
6	182 -10-202-0	63.90	0.533	0.640	15.66	5.34	
6	182 -10-202-1	92.60	0.550	0.654	22.70	8.16	(AR)
7	178 -14-102-0	63.80	0.489	0.587	15.64	4.49	
7	178 -14-102-1	92.30	0.505	0.572	22.62	6.54	(AR)
8	178 -14-201-0	65.50	0.519	0.608	16.05	5.06	
8	178 -14-201-1	93.50	0.529	0.613	22.92	7.43	(AR)
9	165 - 1-101-0	69.00	0.518	0.619	16.91	5.42	
9	165 - 1-101-1	94.30	0.538	0.631	23.11	7.85	(AR)
10	165 - 1-202-0	69.70	0.525	0.614	17.08	5.51	
10	165 - 1-202-1	95.10	0.547	0.632	23.31	8.06	(AR)
11	165 -14-103-0	162.10	0.527	0.634	16.21	5.42	
11	165 -14-103-1	229.00	0.550	0.648	22.90	8.16	(AR)
12	166 - 6-101-0	68.90	0.506	0.481	16.89	4.11	
13	166 - 6-202-0	70.80	0.539	0.747	17.35	6.99	
13	166 - 6-202-1	98.10	0.550	0.741	24.04	9.80	(AR)
14	166 -10-101-0	68.40	0.531	0.685	16.76	6.10	
14	166 -10-101-1	94.80	0.546	0.688	23.24	8.73	(AR)
15	166 -10-202-0	69.40	0.540	0.722	17.01	6.63	
15	166 -10-202-1	97.30	0.552	0.710	23.85	9.35	(AR)
16	166 -15-101-0	66.30	0.508	0.592	16.25	4.89	
17	166 -15-202-0	69.20	0.539	0.694	16.96	6.34	
17	166 -15-202-1	95.40	0.551	0.693	23.38	8.93	(AR)
18	167 - 5-102-0	63.10	0.527	0.614	15.47	5.01	
19	167 - 5-201-0	59.70	0.519	0.610	14.63	4.63	
20	167 - 5-302-0	65.70	0.532	0.708	16.10	6.06	
21	167 -10-101-0	68.00	0.532	0.676	16.67	5.99	
21	167 -10-101-1	92.40	0.542	0.672	22.65	8.25	(AR)

Table 4. Characteristics of Recent Slotted SOC Cells and Their Corresponding Single-Crystal Control Cells (Continued)

item	Cell Number	Isc (mA)	Voc (V)	Fill Factor	Total-Area Jsc (mA/sqcm)	Total-Area Eff. (%)	
22	167 -10-202-0	68.10	0.534	0.687	16.69	6.12	
22	167 -10-202-1	92.30	0.540	0.692	22.62	8.45	(AR)
23	167 -12-102-0	69.20	0.540	0.730	16.96	6.69	
24	167 -13-102-0	64.10	0.516	0.590	15.71	4.78	
25	168 - 8-101-0	71.10	0.540	0.691	17.43	6.50	
25	168 - 8-101-1	98.30	0.557	0.686	24.09	9.21	(AR)
26	168 - 8-202-0	67.00	0.522	0.607	16.42	5.20	
26	168 - 8-202-1	90.00	0.540	0.629	22.06	7.49	(AR)
27	168 - 9-102-0	71.10	0.542	0.748	17.43	7.06	
27	168 - 9-102-1	95.70	0.552	0.739	23.46	9.57	(AR)
28	168 -11-102-0	68.40	0.521	0.637	16.77	5.56	
29	168 -11-201-0	67.10	0.531	0.659	16.45	5.76	
30	168 -12-101-0	66.40	0.535	0.730	16.28	6.36	
30	168 -12-101-1	94.00	0.542	0.732	23.04	9.14	(AR)
31	168 -12-202-0	65.90	0.524	0.642	16.15	5.43	
31	168 -12-202-1	93.10	0.533	0.648	22.82	7.88	(AR)
32	169 - 2-103-0	173.20	0.546	0.679	17.32	6.42	
33	169 - 3-103-0	171.60	0.542	0.717	17.16	6.67	
33	169 - 3-103-1	250.00	0.552	0.706	25.00	9.75	(AR)
34	169 - 5-101-0	67.30	0.527	0.640	16.50	5.56	
35	169 - 5-202-0	68.10	0.537	0.685	16.69	6.14	
36	169 - 6-102-0	68.60	0.529	0.703	16.81	6.25	
36	169 - 6-102-1	94.50	0.548	0.693	23.16	8.80	(AR)
37	169 - 6-201-0	68.00	0.532	0.693	16.67	6.14	
37	169 - 6-201-1	95.10	0.550	0.688	23.31	8.82	(AR)
38	170 - 1-102-0	72.20	0.536	0.678	17.70	6.43	
39	170 - 8-202-0	68.50	0.543	0.734	16.79	6.69	
39	170 - 8-202-1	96.40	0.552	0.718	23.63	9.36	(AR)
40	170 - 9-103-0	168.20	0.537	0.694	16.82	6.27	
41	171 -13-103-0	168.40	0.540	0.695	16.84	6.32	
42	175 - 4-103-0	166.20	0.540	0.672	16.62	6.03	
42	175 - 4-103-1	235.00	0.551	0.683	23.50	8.84	(AR)

Table 4. Characteristics of Recent Slotted SOC Cells and Their Corresponding Single-Crystal Control Cells (Continued)

item	Cell Number	Isc (mA)	Voc (V)	Fill Factor	Total-Area Jsc (mA/sqcm)	Total-Area Eff. (%)	
43	175 - 6-102-0	72.40	0.547	0.737	17.74	7.15	
44	175 - 6-201-0	70.00	0.538	0.669	17.16	6.18	
45	175 - 8-101-0	71.10	0.540	0.708	17.43	6.66	
46	175 - 8-202-0	69.50	0.510	0.450	17.03	3.91	
47	175 -12-101-0	71.80	0.542	0.724	17.60	6.91	
48	175 -12-202-0	71.50	0.523	0.619	17.52	5.67	
49	175 -13-103-0	169.30	0.529	0.650	16.93	5.82	
50	176 - 3-102-0	72.90	0.549	0.740	17.87	7.26	
51	176 - 3-201-0	67.90	0.540	0.678	16.64	6.09	
52	176 - 5-103-0	173.20	0.543	0.716	17.32	6.73	
52	176 - 5-103-1	249.00	0.558	0.713	24.90	9.91	(AR)
53	176 - 7-103-0	174.10	0.532	0.633	17.41	5.86	
54	178 -13-102-0	66.80	0.525	0.638	16.37	5.48	
55	178 -13-201-0	66.80	0.525	0.616	16.37	5.30	
56	426 - 3-101-0	71.20	0.514	0.606	17.45	5.44	
57	426 - 3-202-0	68.00	0.478	0.588	16.67	4.69	
58	426 - 4-103-0	172.90	0.545	0.688	17.29	6.48	
59	183 - 6-102-0	67.80	0.524	0.641	16.62	5.58	
60	183 - 6-201-0	69.30	0.527	0.599	16.99	5.36	
61	183 - 5-102-0	71.90	0.536	0.729	17.62	6.89	
61	183 - 5-102-1	99.20	0.542	0.708	24.31	9.33	(AR)
62	183 - 5-201-0	72.50	0.540	0.708	17.77	6.79	
62	183 - 5-201-1	99.50	0.546	0.692	24.39	9.24	(AR)
63	183 - 7-102-0	71.40	0.539	0.728	17.50	6.87	
63	183 - 7-102-1	99.70	0.547	0.717	24.44	9.58	(AR)
64	183 - 7-201-0	69.50	0.538	0.699	17.03	6.41	
64	183 - 7-201-1	97.80	0.546	0.680	23.97	8.90	(AR)
65	180 - 6-201-0	68.90	0.529	0.668	16.89	5.97	
65	180 - 6-201-1	96.30	0.535	0.652	23.60	8.23	(AR)
66	180 - 5-101-0	72.60	0.537	0.638	17.79	6.10	
66	180 - 5-101-1	100.40	0.545	0.601	24.61	8.06	(AR)

Table 4. Characteristics of Recent Slotted SOC Cells and Their Corresponding Single-Crystal Control Cells (Continued)

item	Cell Number	Isc (mA)	Voc (V)	Fill Factor	Total-Area Jsc (mA/sqcm)	Total-Area Eff. (%)
67	180 - 5-202-0	74.20	0.537	0.660	18.19	6.45
67	180 - 5-202-1	103.40	0.549	0.633	25.34	8.81 (AR)
68	180 - 4-102-0	74.30	0.536	0.726	18.21	7.09
68	180 - 4-102-1	103.40	0.537	0.700	25.34	9.53 (AR)
69	180 - 4-201-0	74.60	0.530	0.644	18.28	6.24
69	180 - 4-201-1	102.80	0.533	0.627	25.20	8.42 (AR)
70	179 - 9-102-0	71.40	0.515	0.721	17.50	6.50
70	179 - 9-102-1	99.90	0.523	0.709	24.49	9.08 (AR)
71	179 - 9-201-0	71.00	0.523	0.698	17.40	6.35
71	179 - 9-201-1	100.80	0.533	0.678	24.71	8.93 (AR)
72	179 -15-102-0	65.90	0.490	0.552	16.15	4.37
72	179 -15-102-1	94.70	0.521	0.516	23.21	6.24 (AR)
73	179 - 4-102-0	74.40	0.514	0.707	18.24	6.63
73	179 - 4-102-1	102.80	0.517	0.659	25.19	8.58 (AR)
74	179 - 4-201-0	74.00	0.519	0.720	18.14	6.78
74	179 - 4-201-1	110.20	0.519	0.681	27.01	9.55 (AR)
75	179 -14-102-0	71.00	0.507	0.654	17.40	5.77
75	179 -14-102-1	95.20	0.518	0.612	23.33	7.40 (AR)
76	179 -14-201-0	71.10	0.513	0.657	17.43	5.87
76	179 -14-201-1	97.60	0.525	0.625	23.92	7.85 (AR)
77	179 - 3-102-0	75.00	0.515	0.710	18.38	6.72
77	179 - 3-102-1	103.10	0.519	0.683	25.27	8.96 (AR)
78	179 - 3-201-0	74.70	0.523	0.700	18.31	6.70
78	179 - 3-201-1	103.70	0.525	0.655	25.42	8.88 (AR)
79	179 -13-102-0	73.10	0.513	0.664	17.92	6.10
79	179 -13-102-1	101.00	0.525	0.626	24.76	8.14 (AR)
80	179 -13-201-0	74.50	0.522	0.670	18.26	6.39
80	179 -13-201-1	102.60	0.533	0.642	25.15	8.60 (AR)
81	184 -12-102-0	67.00	0.504	0.724	16.42	5.99
81	184 -12-102-1	90.30	0.516	0.616	22.13	7.04 (AR)
82	184 -12-201-0	65.00	0.495	0.679	15.93	5.36
82	184 -12-201-1	90.50	0.514	0.652	22.18	7.43 (AR)
83	184 - 8-101-0	65.80	0.490	0.659	16.13	5.21
83	184 - 8-101-1	91.60	0.509	0.641	22.45	7.32 (AR)

Table 4. Characteristics of Recent Slotted SOC Cells and Their Corresponding Single-Crystal Control Cells (Concluded)

item	Cell Number	Isc (mA)	Voc (V)	Fill Factor	Total-Area Jsc (mA/sqcm)	Total-Area Eff. (%)	
84	184 - 8-202-0	67.30	0.493	0.679	16.49	5.52	
84	184 - 8-202-1	97.20	0.512	0.656	23.82	8.00	(AR)
85	184 -10-102-0	68.20	0.501	0.487	16.72	4.08	
85	184 -10-102-1	87.60	0.518	0.445	21.47	4.95	(AR)
86	184 -10-201-0	72.70	0.492	0.570	17.82	4.99	
86	184 -10-201-1	95.30	0.504	0.532	23.36	6.26	(AR)
(Single-Crystal)							
87	Q67A- 0-102-0	87.40	0.569	0.761	21.42	9.28	
88	Q67A- 0-201-0	86.20	0.537	0.745	21.13	8.45	
89	Q67B- 0-102-0	90.10	0.560	0.744	22.06	9.19	
90	Q67B- 0-201-0	88.10	0.552	0.735	21.59	8.76	
91	Q68A- 0-102-0	85.50	0.562	0.753	20.96	8.87	
92	Q68A- 0-201-0	86.10	0.561	0.749	21.10	8.87	
93	Q70A- 0-102-0	87.20	0.560	0.782	21.37	9.36	
94	Q70A- 0-201-0	86.70	0.560	0.760	21.25	9.04	
95	Q70B- 0-102-0	87.10	0.561	0.760	21.35	9.10	
96	Q71A- 0-101-0	87.60	0.564	0.769	21.47	9.31	
97	Q71A- 0-202-0	89.80	0.566	0.770	22.01	9.59	
98	Q72B- 0-102-0	89.50	0.558	0.735	21.94	9.00	
99	Q72B- 0-201-0	87.00	0.561	0.745	21.32	8.91	
100	Q76A- 0-102-0	88.50	0.565	0.764	21.69	9.36	
101	Q79 - 0-102-0	89.30	0.558	0.765	21.89	9.35	
102	Q80A- 0-102-0	86.00	0.561	0.765	21.08	9.05	
103	Q80B- 0-102-0	87.00	0.565	0.773	21.32	9.31	
104	R3A - 0-102-0	86.80	0.556	0.758	21.28	8.97	
105	R3A - 0-201-0	86.30	0.551	0.755	21.15	8.80	
106	R5 - 0-102-0	90.60	0.543	0.739	22.21	8.91	
107	R6 - 0-102-0	89.10	0.543	0.659	21.84	7.82	
108	R7 - 0-102-0	88.20	0.542	0.755	21.62	8.85	

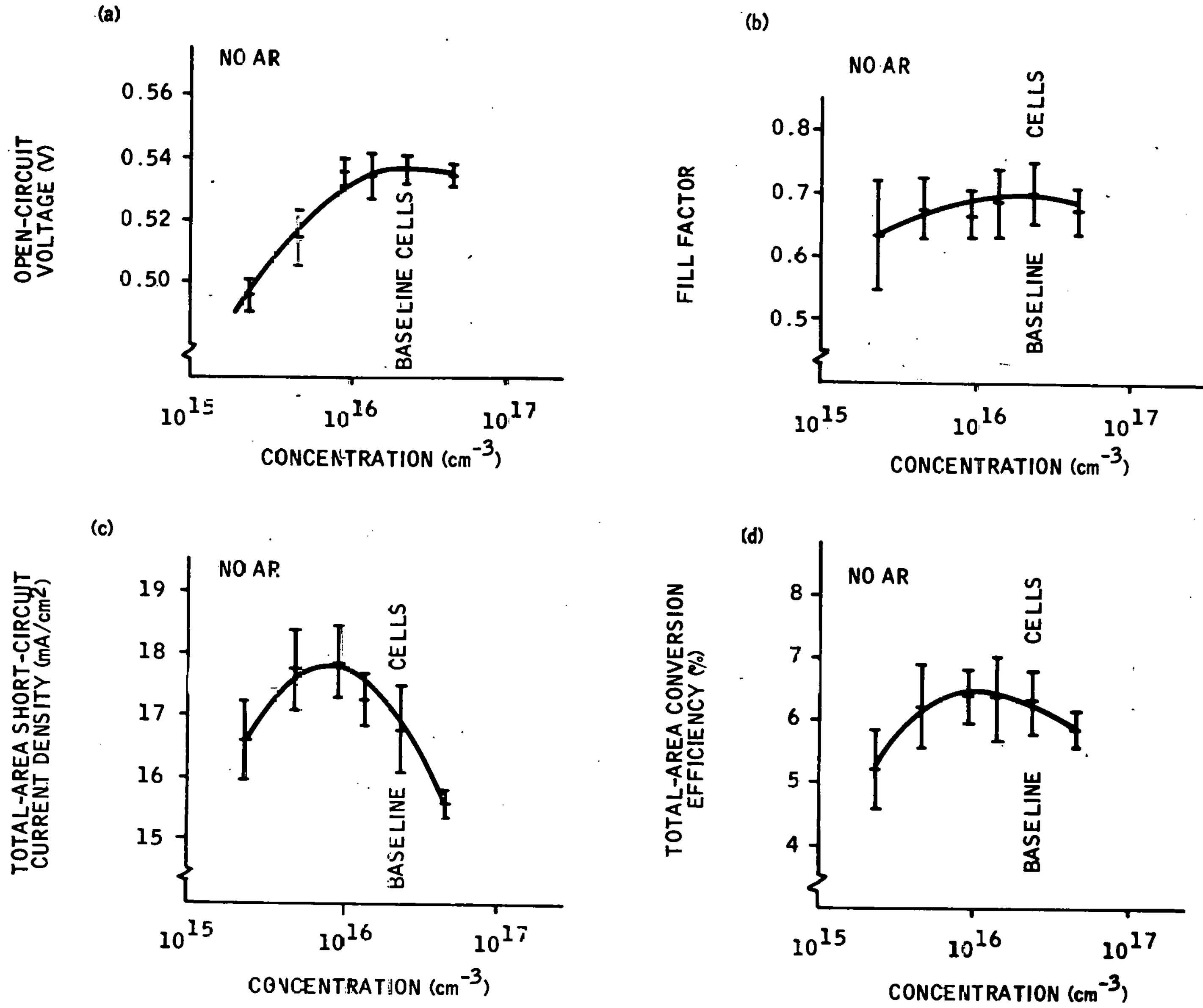

Figure 7. Performance of Slotted SOC Cells as a Function of Base Doping Concentration, for Cells without AR Coating

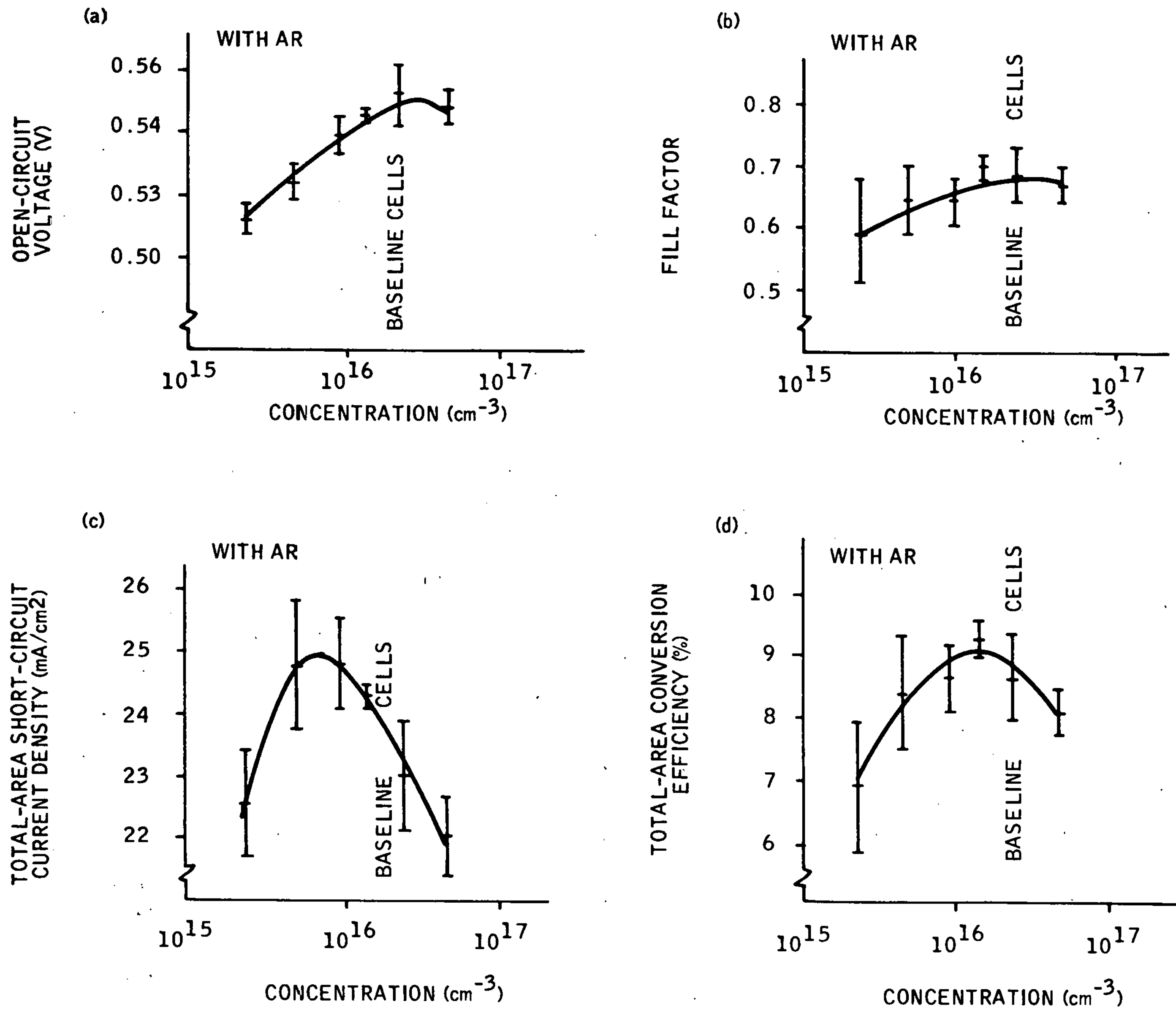

Figure 8. Performance of Slotted SOC Cells as a Function of Base Doping Concentration, for Cells with AR Coating

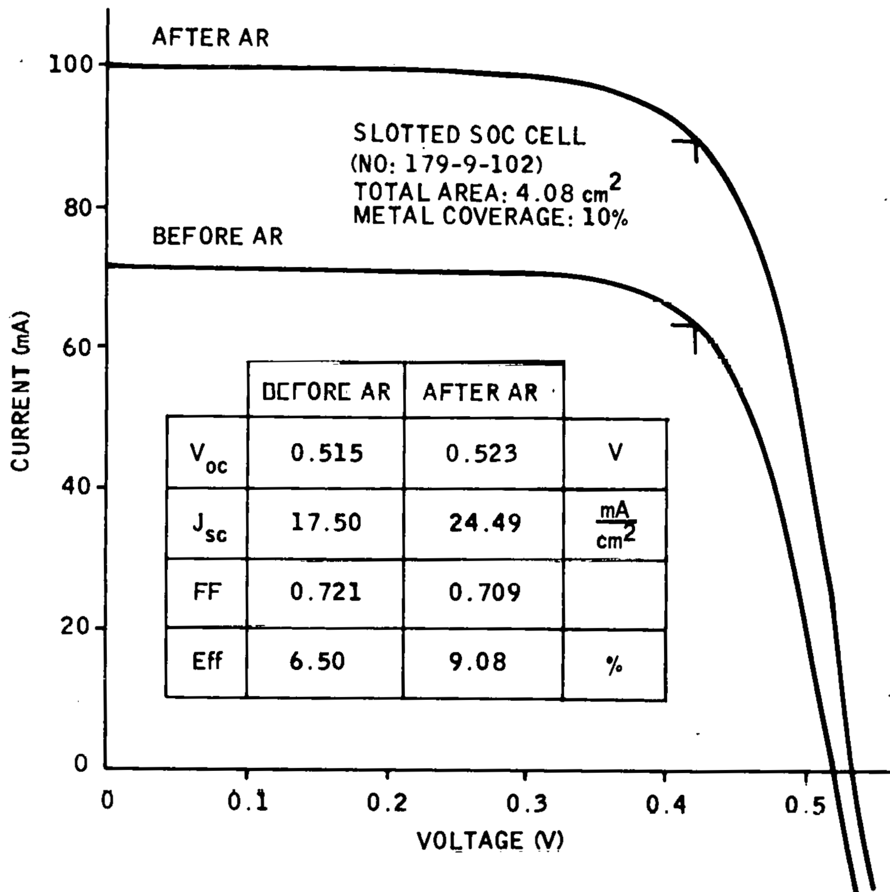

	BEFORE AR	AFTER AR	
V_{oc}	0.515	0.523	V
J_{sc}	17.50	24.49	$\frac{mA}{cm^2}$
FF	0.721	0.709	
Eff	6.50	9.08	%

Figure 9. Current-Voltage Characteristics of a Slotted SOC Cell Made from Material Grown at 0.08 cm/sec

Calculated Values of Series Resistance

With the present trend toward reducing the base doping concentration and toward increasing growth speed, the parasitic series resistance of future SOC cells will certainly be greater than that of present cells. Fortunately, the performance of slotted SOC cells will not be substantially affected by the expected values of series resistances, as will be demonstrated by the calculations given in this and the following sections.

The parasitic series resistance, R_P, can be divided into three components· the front contact resistance, R_c', the silicon layer resistance, R_L', and the back layer resistance,

R_L. The back contact resistance can be neglected. The gront contact resistance R'_C is assumed to be given by

$$R'_C = R'_\ell / \ell \qquad (1)$$

where ℓ is the peripheral length of the emitter metalization pattern and R'_ℓ is the specific contact resistance in ohms-cm. An accurate value of R_ℓ is not known; we assume here that R'_ℓ = 0.3 ohm/cm. Thus, R'_C = 0.013 ohm, since ℓ = 24 cm. The front silicon layer resistance, R'_L, is given by

$$R'_L = \frac{1}{12} R'_\square \left(\frac{b' - k'}{N' w} \right) \qquad (2)$$

where $R_\square$ is the front later sheet resistance in ohms/square, b' is the unit cell width, k' is the width of a contact finger, N' is the number of unit cells per solar cell and w is the width of the solar cell. For a typical SOC cell, $R'_\square$ = 50 ohms/square, b' = 0.34 cm, k' = 0.03 cm, N' = 7.06, and w = 1.7 cm, given that R'_L = 0.108 ohm. For the back layer resistance, R_L, we use the following equation:

$$R_L = \frac{R_\square}{(Nb)w} \left[\frac{b^2}{12} \left(1 - \frac{d}{b}\right)^{2\ 2} + h^2 \left(\frac{b}{d}\right) \right] \qquad (3)$$

Where $R_\square$ is the sheet resistance of the back layer, b is the center-to-center distance between slots, d is the slot width, h is the thickness of the back layer, N is the number of slots per solar cell, and w is the width of the solar cell. Thus, (Nb)w is the total area of the solar cell. By making two assumptions, we can rewrite Equation (3) in terms of base doping concentration, N_{BG}, and growth speed, v First, we assume that base sheet resistivity which equals $R_\square h$ is inversely proportional to N_{BG}. Thus

$$R_\square h = K/N_{BC} \qquad (4)$$

where K is an empirical constant. For SOC material with a base doping concentration, N_{BG}, of $2.3 \times 10^{16}/cm^3$, $R_\square h$ is about 1 Ω-cm, given that K = $2.3 \times 10^{16}/cm^3$ Second, we assume that the silicon thickness, h, is inversely proportional to the square of the growth velocity, v. Thus,

$$h = K^*/v^2 \qquad (5)$$

where K- is an empirical constant. For a growth speed of 0.06 cm/sec, h is about 200 μm. Thus K* is about 7.2×10^{-5} cm^3 For a typical SOC cell, b = 0.25 cm, d = 0.1 cm, and (Nb)w = 4.08 cm^2, so that equations (3) and (4) combine to give

$$R_L = \frac{1.49 \times 10^{13}}{N_{BG}} \left(v^2 + \frac{6.91 \times 10^{-6}}{v^2} \right) \tag{6}$$

Because the total parasitic, R_P, equals $R'_C + R'_L + R_L$, the specific series resistance, R_PA, is given by

$$R_PA = 0.494 + \frac{6.07 \times 10^{13}}{N_{BG}} \left(v^2 + \frac{6.91 \times 10^{-6}}{v^2} \right) \tag{7}$$

since $A = 4.08\ cm^2$. Equation (7) yields the data in Table 5.

Table 5. Specific Series Resistance versus Base Doping Concentration and Thickness

v (cm/sec)	h (μm)	Specific Series Resistance (Ω-cm^2)		
		Base Doping Concentration (cm^{-3})		
		2.3×10^{16}	10^{16}	4.7×10^{15}
0.06	200	0.64*	0.83	1.21
0.07	147	0.66	0.88**	1.31
0.08	113	0.69	0.95	1.46

*Conditions for 1978 baseline cells.
**New standard conditions.

For the new standard base doping concentration of $10^{16}/cm^3$ and the new standard growth velocity of 0.97 cm/sec, the calculated specific series resistance is ~0.88 ohm-cm^2, compared with a calculated value of ~0.64 for the 1978 baseline cells.

Effects of Series Resistance

To investigate the relationship between cell performance and specific series resistance, we begin by assuming that the present SOC cell characteristics can be calculated using an equation of the following form:

$$I = I_{01} \left[\exp \frac{q(V - IR_s)}{kT} - 1 \right] + I_{02} \left[\exp \frac{q(V - IR_s)}{nkT} - 1 \right] + \frac{V - IR_s}{R_{sh}} - I_{sc} \tag{8}$$

where the various parameters were defined in Quarterly Report No. 11. For an example, consider SOC cell No. 180-4-102-1. The dark and light current-voltage characteristics are given in Figures 10 and 11, respectively. Using the methods given in Quarterly Report No. 11, the dark characteristic yields the data in Table 6.

Table 6. Fitted Parameters for SOC Cell No. 180-4-102-1

Parameter	Value
R_{sh}	100 kΩ
n	1.7
I_{02}	8.85×10^{-5} mA
I_{01}	8.9×10^{-8} mA
A	4.08 cm^2
R_pA	2.1 Ω-cm^2
J_{02}	2.2×10^{-5} mA/cm^2
J_{01}	2.19×10^{-8} mA/cm^2

From the light characteristics, the total-area short-circuit current, I_{sc}, is 101.2 mA. This value, the values given in Table 5, and Equation (8) give the calculated points shown in Figure 11. For this example, there is good agreement between theory and experiment.

To investigate how series resistance affects cell performance, we now repeat the just given calculation for different values of specific series resistance. The results are given in Figure 12. The calculated efficiency is 10.6 percent for $R_sA = 0$, 10.1 percent for $R_sA = 0.83$ Ω-cm^2.

The first case corresponds to zero series resistance; the second case corresponds to the calculated value of series resistance for $N_{BG} = 10^{16}/cm^3$ and v = 0.06 cm/sec; and the third case corresponds to the measured value of series resistance. Thus, for this example, using cell 180-4-102-1, the conversion efficiency would be 10.1 percent rather than 9.5 percent, if the measured value of series resistance were equal to the calculated value.

MATERIAL EVALUATION (D. Zook and R. Hegel)

During the past quarter, the evaluation effort emphasized the measurement of diffusion length and grain boundary effects using the LBIC method. The electrolyte technique has been improved by the use of a smaller light-beam spot size, yielding resolution comparable

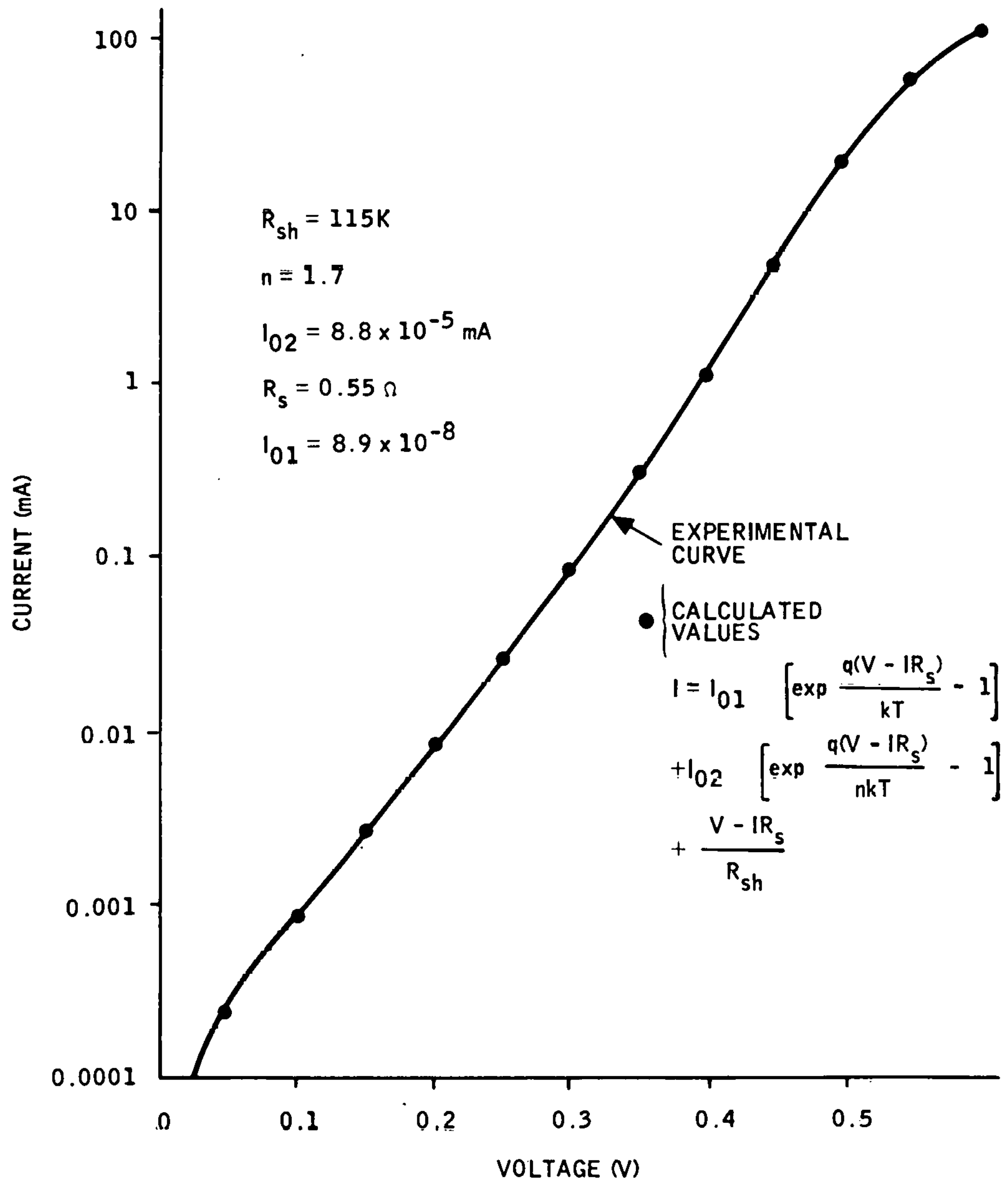

Figure 10. Dark Characteristics of SOC Cell No. 108-4-102-1

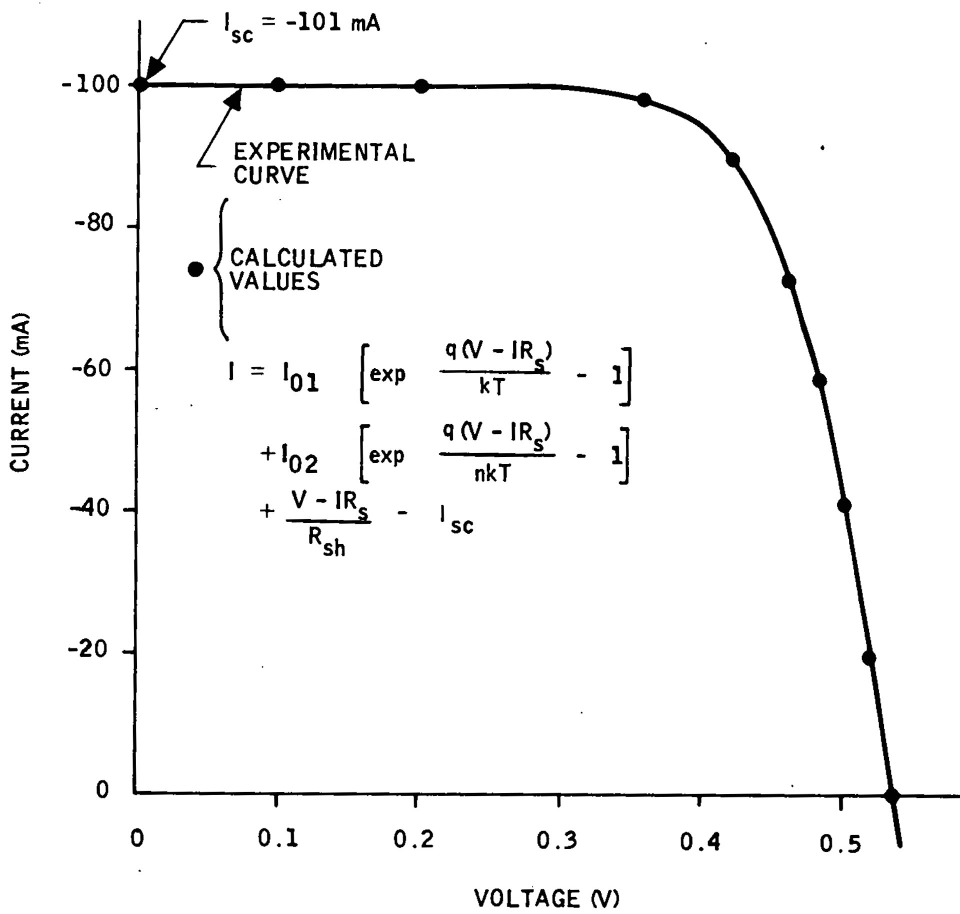

Figure 11. Light Current-Voltage Characteristics for SOC Cell No. 180-4-102-1. The calculated values were based on the dark-current fit and the value of I_{sc}.

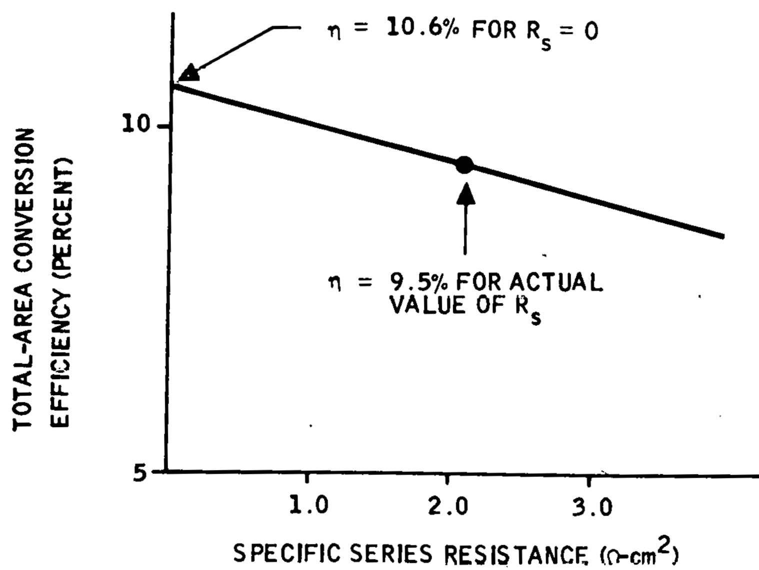

Figure 12. Conversion Efficiency as a Function of Specific Series Resistance

to that obtained with p-n junctions. The spot size is now about 6 μm wide and 15 μm long. The narrow dimension is scanned across the width of the sample. Since the grain boundaries are nearly parallel to the growth axis, the resolution with which a grain boundary can be scanned is about 6 μm. A magnified LBIC scan of a grain boundary in a SCIM-coated sample is shown in Figure 13. The diffusion length was evaluated, given the value of L_n = 34 ± 3 μm at the spot labeled "L_n data." This value is comparable to the values measured in dip-coated material.

The electrolyte technique has been used to correlate the minority carrier diffusion length, L_n, with the dip number. Dip Run 185 was lightly doped (2×10^{15} boron atoms/cm^3) and 23 substrates were dip coated at the same growth rate (0.06 cm/sec) and melt temperature. Because of the light doping, the resistivity of the layers also was expected to change with dip number.

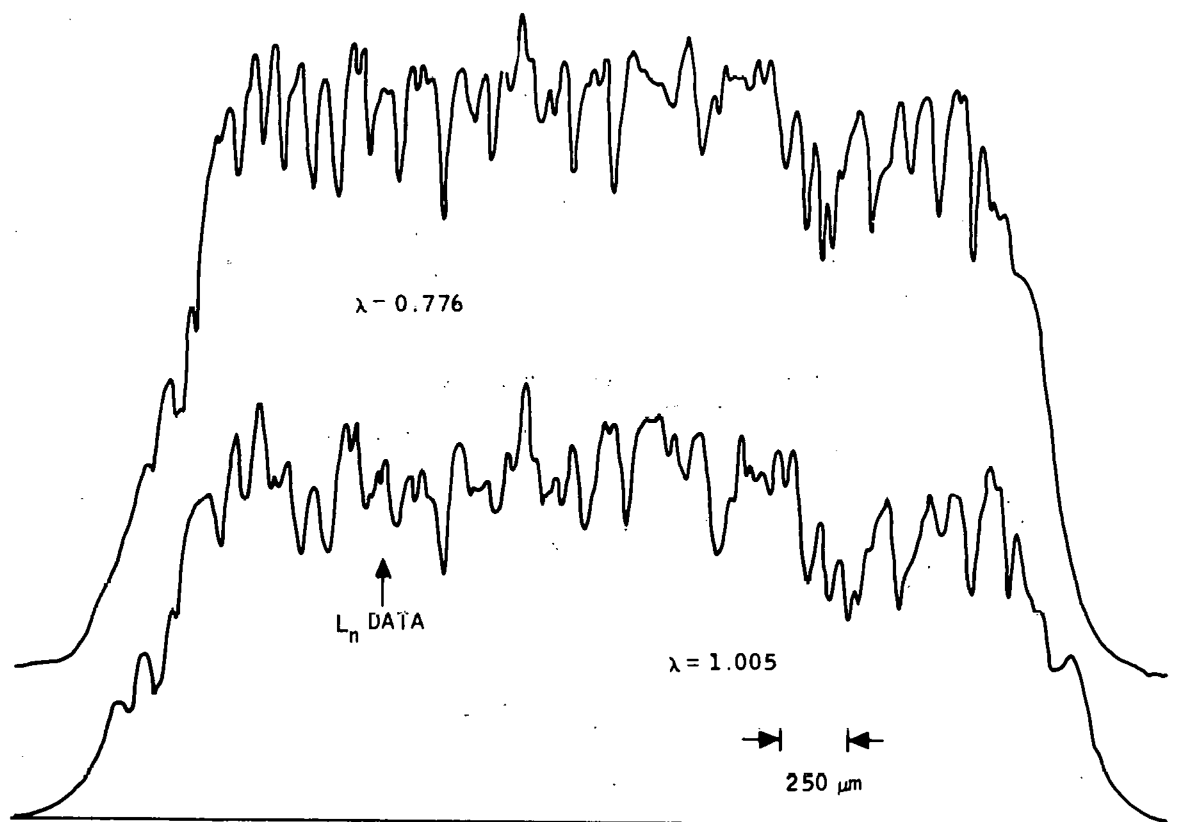

Figure 13. LBIC Scans of a SCIM-Coated SOC Sample Taken by the Electrolyte Method. The light beam spot size is about 6 μm. The drop in current at the edge of the scan is caused by vignetting of the light beam by the platinum electrode which is out of focus.

The diffusion length was determined in the following way. A region with large grain size was selected and the electrolyte electrode was mounted so that only a few grains were in the region to be scanned (3mm diameter). The region was scanned at several infrared wavelengths, as illustrated in Figure 13. For the most part, the scans snowed uniform regions with sharp dips associated with low-angle grain boundaries.

A uniform region showing "average" response at 1.0 μm was selected and the LBIC response was measured using the procedure described previously (i.e., using chopped light at 50 cycles and a 15 μm spot size).

The results are shown in Figure 14. Both the diffusion length, L_n, and the sheet resistance, ρ_s, decreased by a factor of 2 during the dipping sequence. The decrease in ρ_s is very likely due to aluminum, whereas the decrease in L_n is probably due to transition metal impurities (e.g., Fe, Ti, and V). The fact that both changed by a factor of 2 is fortuitous, in view of the fact that the two parameters should depend on impurity concentration in different ways.

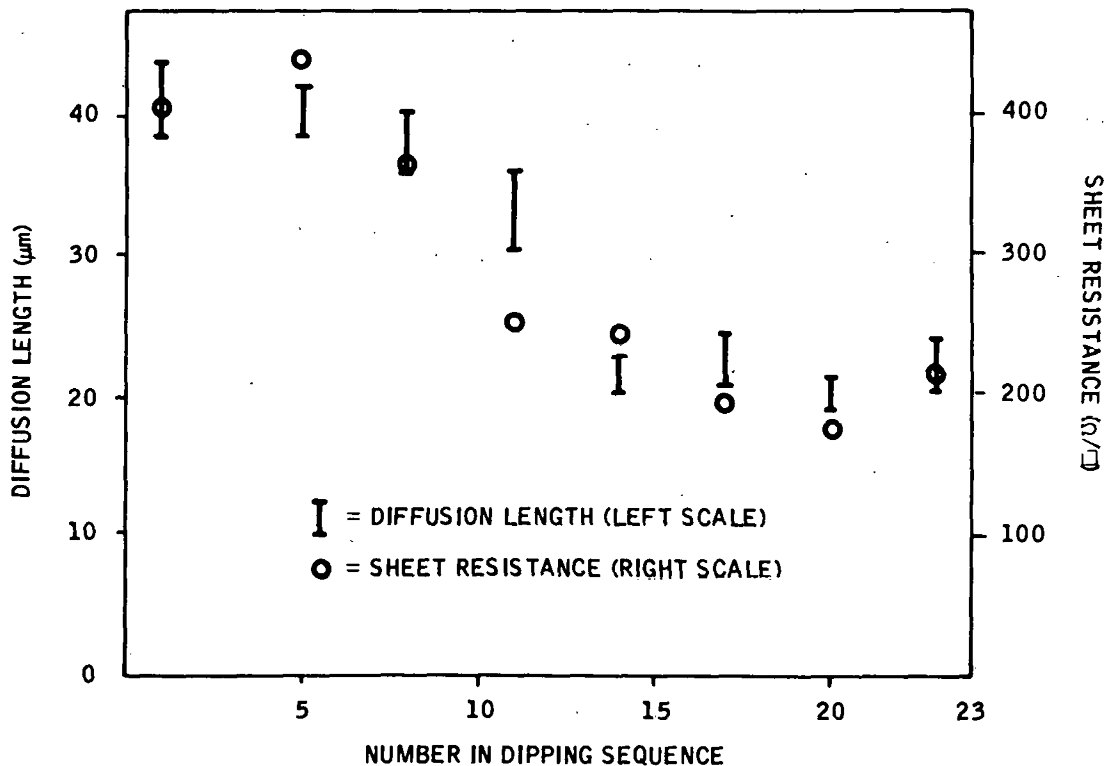

Figure 14. Diffusion Length, L_n, with Grains and Sheet Resistance, ρ_s, as Functions of the Dip Number for Dip Run 185

Loss in Short-Circuit Current Due to a Grain Boundary

The simplest model of a grain boundary is a surface with infinite recombination velocity, clearly the "worst-case" situation. The basic theory follows from the work of van Roosbroeck,[2] who developed the theory of the effect of surface recombination on current collection by a p-n junction. Theoretical work[3, 4] on the effect of a scanning electron microscope electron-beam-induced currents (EBIC), based on Ref. 2, is also relevant to the light-beam-induced current (LBIC) case.

We consider the geometry shown in Figure 15, with the grain boundary at right angles to the junction. The coordinate system is the same one used by Refs. 2 through 4. A point source produces four minority carriers, n, at the point (x_s, z_s), and the boundary conditions are n = 0 at x = 0 (the p-n junction) and z = 0 (the grain boundary) and can be met with image sources as shown. The incoming light ray is a line source which is a distance z_s from the grain boundary, with source strength $g = \alpha e^{-\alpha x}$, where α is the absorption coefficient of the light. As discussed by van Roosbroeck, the same junction collection efficiency is obtained whether the point (x_s, z_s) represents a point source or an infinite line source parallel to the y-axis through the point (x_s, z_s). The Green's function for single line source is given by van Roosbroeck as:

$$n_1\ (X, Z;\ X_s Z_s) = \frac{1}{2\pi}\frac{R_1}{D_o} K_o\left[\sqrt{(X - X)^2 + (Z - Z_s)^2}\right] \qquad (9)$$

where K_o is a modified Bessel function of the second kind. Here D_o is the electron diffusivity, R_1 is generation rate per unit length, and the capital letters for the coordinates mean the value normalized to the diffusion length, L, (e.g., X = x/L). The carrier density due to the three image points is similar to Equation (9) and the total value of n is the sum of the four terms.

The corresponding efficiency for charge collection by the p-n junction is given by:[2]

$$Q_1(X_s,\ Z_s) = \frac{D_o}{R_1}\int_o^{\infty} \left.\frac{\partial n}{\partial X}\right|_{X=0} dZ \qquad (10)$$

Noting that $dK_o(R)/dR = -K_1(R)$, we see that

$$Q_1(X_s, Z_s) = \frac{X_s}{2\pi}\int_o^{\infty} dZ\ \frac{K_1\left(\sqrt{X_s^2 + (Z - Z_s)^2}\right)}{\sqrt{X_s^2 + (Z - Z_s)^2}} \qquad (11)$$

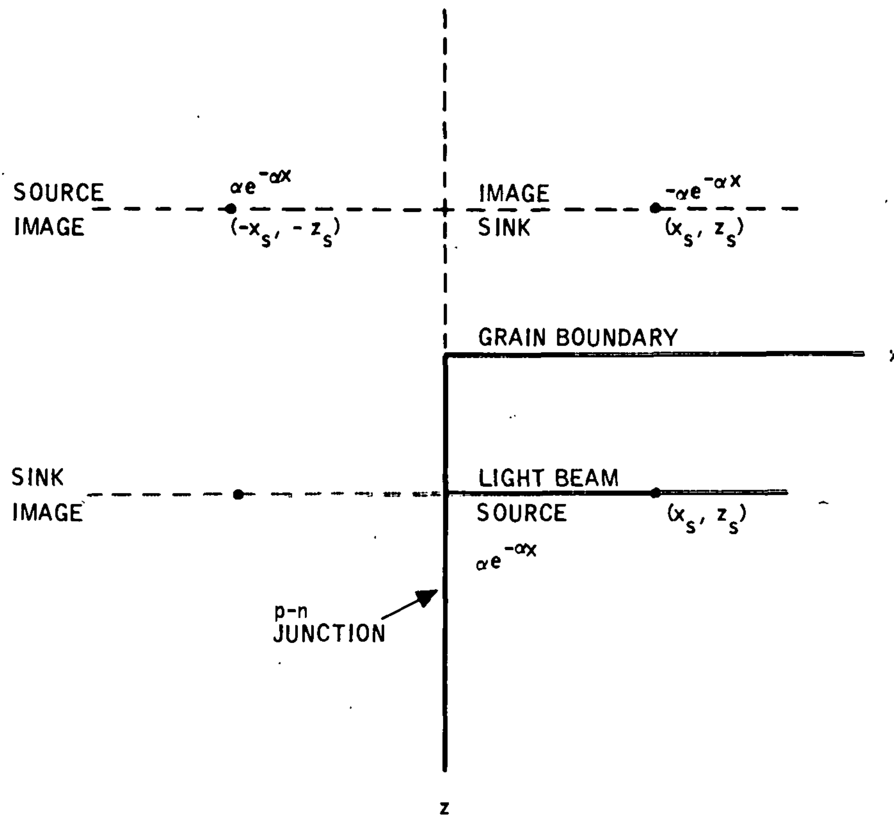

Figure 15. Geometry Used for Analysis of Grain Boundary Effects on Light Beam Response

The integration can be simplified by making use of the Sonine formula:[2]

$$\int_0^\infty \frac{K_1\left(\sqrt{X_s^2 + Z^2}\right)}{\sqrt{X_s^2 + Z^2}}\, dZ = \frac{1}{2}\, e^{-X_s} \tag{12}$$

This relationship illustrates the fact that a point source or a line source will produce a current across a plane a distance x away from a quantum efficiency $\frac{1}{2}\, e^{-x/L}$. If the plane is a p-n junction, then there is an equal current from the image source, so that the quantum efficiency is simply

$$2Q_1(X_s, 0) = e^{-X_s} = e^{-x_s/L} \tag{13}$$

Using Equation (12), we can rewrite Equation (11) as:

$$Q_1(X_s, Z_s) = \frac{1}{2}e^{-X_s} + \frac{X_s}{2\pi}\int_0^{Z_s} dZ \, \frac{K_1\left(\sqrt{X_s^2 + Z^2}\right)}{\sqrt{X_x^2 + Z^2}} \tag{14}$$

Analogously,

$$Q_4(X_s, -Z_s) = -\frac{1}{2}e^{-X_s} + \frac{X_s}{2\pi}\int_0^{Z_s} dZ \, \frac{K_1\left(\sqrt{X_s^2 + Z^2}\right)}{\sqrt{X_s^2 + Z^2}} \tag{15}$$

giving a net negative current, since it represents a sink rather than a source.

Summing the contributions from the four points at $(\pm X_s, +Z_s)$ in Figure 15 gives

$$Q(X_s, Z_s) = \frac{2}{\pi} X_s \int_0^{Z_s} dZ \, \frac{K_1\left(\sqrt{X_s^2 + Z^2}\right)}{\sqrt{X_s^2 + Z^2}} \tag{16}$$

Using Equation (9) of Ref. 3, it follows that

$$Q(X_s, \infty) = e^{-X_s} \tag{17}$$

which is consistent with Equation (12) above.

The final result for a beam of light traveling along the x-axis a distance Z_s from the grain boundary at $Z = 0$ is

$$Q(Z_s) = \alpha \int_0^{\infty} dx \, e^{-\alpha x} \, Q(\tfrac{x}{L}, Z_s)$$

$$= \frac{2}{\pi}\alpha L \int_0^{\infty} X_s dX_s e^{-\alpha L X_s} \int_0^{Z_s} dZ \, \frac{K_1\left(\sqrt{X_s^2 + Z^2}\right)}{\sqrt{X_s^2 + Z^2}} \tag{18}$$

This result can be simplified by changing the order of integration:

$$Q(Z_s) = \frac{2}{\pi}(\alpha L)\int_0^{Z_s} dZ \int_0^{\infty} XdX\, e^{-\alpha LX}\, \frac{K_1\left(\sqrt{X^2+Z^2}\right)}{\sqrt{X^2+Z^2}}$$

$$= 2\alpha L \int_0^{Z_s} dZ\ G_2(Z) \tag{19}$$

where $G_2(Z)$ is the function $\overline{G}_2$ (0, 0; Z,0) given by van Roosbroeck [Equation (37), Ref. 2] for the surface concentration due to a steady surface line source at a reduced distance Z from the junction. The parameter S relating to surface recombination in Ref. 2 is replaced by αL in Equation (19). The function $G_2(Z)$ is plotted as Figure 7 in Ref. 2.

It is clear from Equations (16) and (18) that $Q(0) = 0$, which means that the quantum efficiency at the grain boundary is zero. This would only be true for a light beam of zero width, however, and it is clear from Figure 2 of Ref. 2 that the finite size of the light beam becomes increasingly important for large values of αL. It follows from Equation (17) that

$$Q(\infty) = \alpha L \int_0^{\infty} dX_s\, e^{-\alpha L X_s}\, e^{-X_s}$$

$$= \frac{\alpha L}{1+\alpha L} \tag{20}$$

This is the quantum efficiency far away from a grain boundary, and is the usual expression for a uniform material of infinite thickness.

The relative change in quantum efficiency is given by combining Equations (19) and (20):

$$\frac{Q(Z/L)}{Q(\infty)} = 1 - 2(1+\alpha L)\int_{z/L}^{\infty} G_2(z)\, dZ \tag{21}$$

where the integral is plotted as Figure 4 in Ref. 2, using the different variables noted above. Equation (21) is plotted in Figure 16 using the curves from Ref. 2 for the integral. Figure 16 actually gives the calculated LBIC line shape for infinite grain boundary recombination velocity in the limit of zero spot size of the light beam. An actual light beam has a finite width, and so the shape would be a smoothed version of the curve in Figure 16.

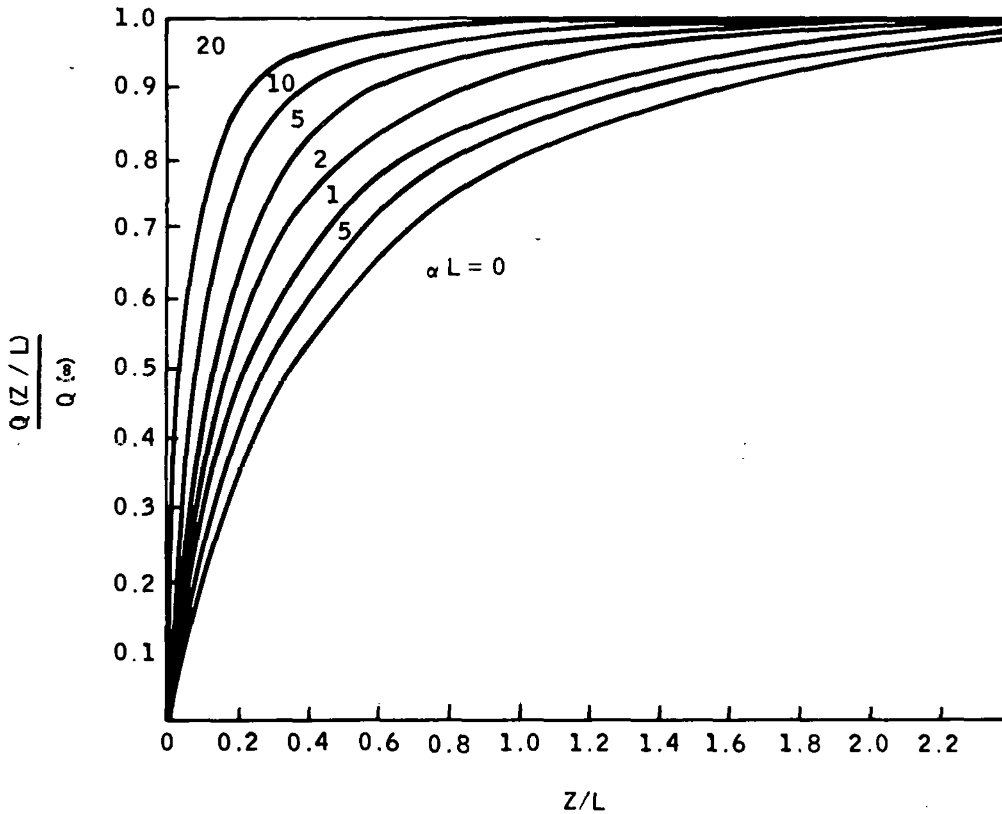

Figure 16. Calculated LBIC Response at a Grain Boundary Having Infinite Surface Recombination Velocity. The light beam spot size is assumed to be zero.

In practice, it is difficult to compare the calculated line shape with the theoretical line shape because of the finite width of the beam. The quantity of most interest for solar cell performance is the loss in short-circuit current due to a grain boundary, compared with the regions within grains. This quantity is

$$w = 2\int_{o}^{\infty} dZ \left| 1 - \frac{Q(Z/L)}{Q(\infty)} \right| = 4(1+\alpha L) \int_{o}^{\infty} dZ \int_{Z'/L}^{\infty} G_2(z')dZ' \tag{22}$$

The factor of 2 enters on the left of the equation because only one-half of the grain boundary is included in the above analysis (only one-half of the LBIC line shape is shown in Figure 16). The quantity w is an effective width of the grain boundary, such that the loss in current due to the grain boundary is equivalent to a loss in cell area of that width times the length of the grain boundary.

The effective width, w, is plotted in Figure 17 as a function of αL. Since αL can vary from zero to infinity, it is convenient to plot as a function of $1 + \alpha L$. The effective width is approximately equal to:

$$w_1 \simeq \frac{3.3L}{1 + \alpha L} \, e^{-\frac{1}{1 + \alpha L}} \tag{23}$$

which is accurate within ±10 percent over the entire range of αL.

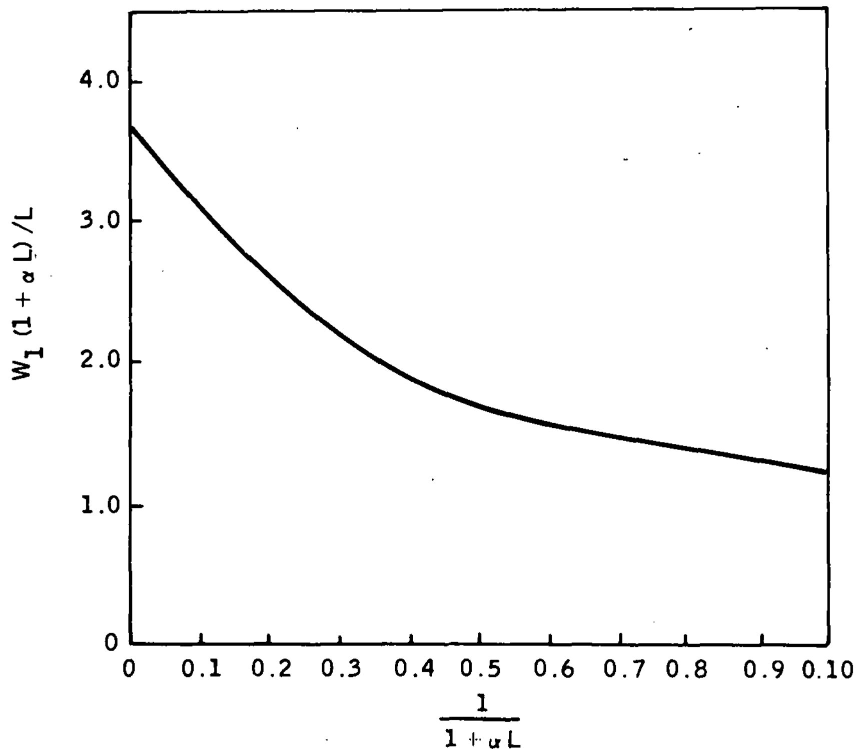

Figure 17. Effective Grain Boundary Width, w, as a Function of α L

Equation (23) is in a form which can conveniently be compared with LBIC experiments. The loss in current at any wavelength due to a grain boundary can be obtained by integrating over the LBIC line shape. The spot size of the scanning light beam is not important as long as it is small compared with the diffusion length. This process has been done for isolated grain boundaries on several LBIC scans, and the results are in reasonable agreement with Equation (23) if the value of L that is used is the value of the background in the vicinity of the grain boundary. This value of L is determined by the relative response to the 1.0 µm scan, since this scan can essentially be considered a mapping of the effective diffusion length within the cell.

We conclude that this analysis, which is still preliminary, is consistent with grain boundaries in our SOC cells having infinite surface recombination velocity. Further studies and modeling will be conducted to verify this conclusion and consider the implication of these results for solar cell performance.

GROWTH MODELING (S. B. Schuldt)

The growth of sheet silicon or silicon ribbon from the melt can happen, in principle, in either of two modes, as illustrated in Figure 18. In the conventional mode (a), the liquid-solid interface (LSI) is oriented approximately perpendicular to the pull direction. The latent heat of fusion released at the LSI is carried in the pull direction and must be disposed of by radiation and convection to the relatively cool environment of the solid ribbon. The word "symmetric" fits this mode because of the plane of symmetry through the half-thickness points. The other mode (b) lacks a plane of symmetry, as diagrammed here, and may be called "asymmetric." Because the LSI is inclined at a small angle, θ, to the pull direction, most of the latent heat of fusion is eliminated immediately by crossing transversely to the free solid surface. Only a small fraction of the latent heat remains to be disposed of downstream (upwards as represented in Figure 18 from the solidification wedge. It is debatable whether asymmetric growth has ever been successfully demonstrated, but it is a critically important technology to pursue theoretically and experimentally. It is inherently much faster than symmetric growth and may have other advantages such as entrapment of impurities.

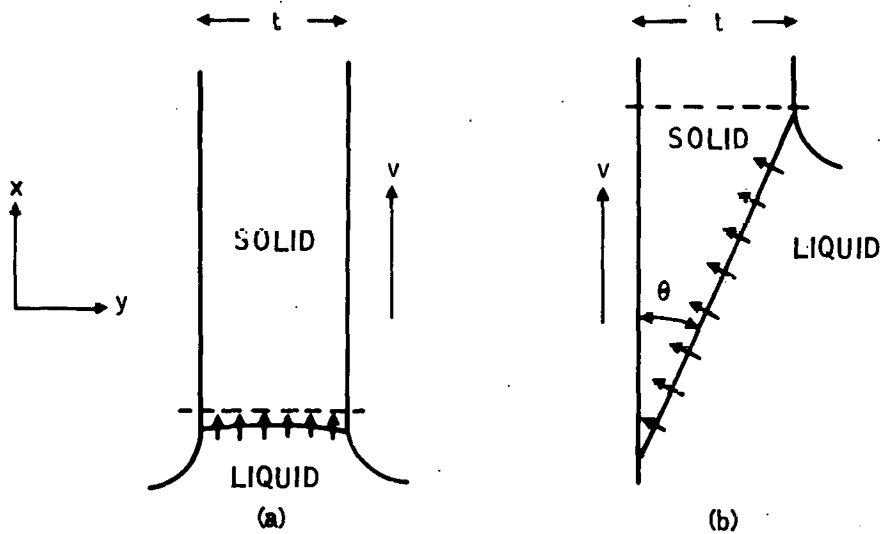

Figure 18. Silicon Ribbon Growth in (a) Symmetric and (b) Asymmetric Modes. The letters v and t are pull speed and ribbon thickness, respectively.

A heat transfer model was developed for the wedge-shaped region[5] in asymmetric growth but it does not address the problem of how to cool the ribbon as it travels away from this region. This report indicates that downstream cooling is too rapid for pure wedge-shaped asymmetric growth if a 300°K ambient is assumed for the entire solid ribbon. The cooling can be retarded to the proper rate by including postheaters in the apparatus. The present analysis applies directly to unsupported ribbon growth. Extension to supported sheet growth, as in silicon-on-ceramic, will be done at a later time.

In both symmetric and asymmetric growth, it is useful to consider lines of demarcation between the solidification zones and the fully developed solid, downstream regions. These are indicated as dashed lines in Figure 18. The heat flux approaching the line from below, consisting of convected heat, heat flux from the liquid, and any latent heat of fusion not already disposed of, must balance the heat flux away from the line into the downstream region. This simple conservation principle leads to a v versus t tradeoff in the case of symmetric growth, as reviewed briefly below. In the asymmetric growth model, the conservation of heat flux does not imply any direct tradeoff limitation, but it does dictate the use of postheaters.

Review of Symmetric Growth Model

The conservation principle for symmetric growth can be expressed

$$t(\rho c v T_F + J_o + \rho L v) = t(kq + \rho c v T_F) \qquad (24)$$

where ρ and c are the density and heat capacity of solid silicon at $T \sim T_F$, T_F is the melting temperature, J_o the x-component of heat flux density in the liquid, L is the latent heat of fusion, k is the heat conductivity of solid silicon (independent of temperature in this analysis), and $q = -dT/dx$, the downstream component of the temperature gradient at the dotted line in Figure 18(a). Values used in this report are given in Table 7. The first term in Equation (24) represents convected heat flux, the second term is the heat flux from the liquid silicon, and the third term is heat flux due to latent heat of fusion. The tkq term is heat flux by conduction into the downstream solid region. Note that convected heat cancels in Equation (24). If J_o is assumed equal to zero (maximum throughput), the equation becomes

$$\rho L v/k = q\Big|_{T=T_F} \qquad (24a)$$

Table 7. Values for Silicon Parameters

Parameter	Value
ρ	$2.33\ g/cm^3$
c	0.954 J/g deg
k	0.216 W cm/deg
L	1802 J/g
T_F	1685 deg K
J_o	$0.0\ W/cm^2$

The value of q is derived independent of the solidification zone parameters by integrating the heat equation for the downstream silicon portion, subject to appropriate initial condition. Since symmetric growth is very nearly one-dimensional in character, the following heat equation is convenient to use:[6]

$$t(k\, q\frac{dq}{dT} + \rho\, cv\, q) = F(T,\ T_A) \qquad (25)$$

where F is the cooling function depending on the ribbon temperature, T, and effective ambient temperature, T_A. This equation is equivalent to the standard one-dimensional heat equation in which the coordinate x is the independent variable. The transformation was made by substituting -q for dT/dx. If heat disposal is by radiation from both surfaces to an effective 300°K blackbody ambient, Equation (25) becomes

$$t(kq\frac{dq}{dT} + \rho cv\, q) = 2\epsilon\sigma\,(T^4 - 300^4) \qquad (26)$$

The initial condition is that the gradient, q, tends to zero as T approaches ambient, i.e., q(300) = 0. The solid silicon emissivity is taken to be $\epsilon = 0.46$, and Equation (26) is integrated numerically[7] from $T = T_A$ to $T = T_F$, since $q(T_F)$ is the value required in Equation (24a).

The q obtained from the integration depends upon t, and to a lesser extent upon v due to the convective term in Equation (26). Figure 19 is a plot of q versus t for various pull speeds, along with $\rho Lv/k$ (dashed lines). The intersections of the two sets, marked with heavy dots, reveal the v versus t tradeoff and illustrate the flux conservation principle.

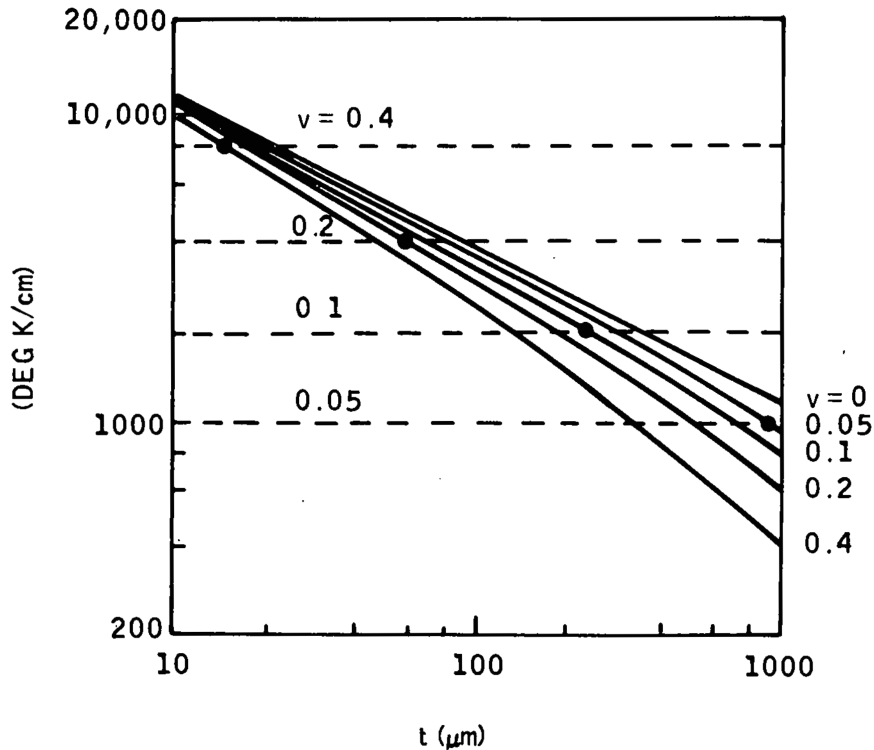

Figure 19. Heat Fluxes from Solidification Region (Dashed) and into Downstream Region (Solid). Balance is at the intersection points (heavy data), establishing the v versus t tradeoff for symmetric growth.

Ribbon Thickness in Asymmetric Growth

A thermal model of asymmetric growth is independent of orientation, and the pull direction has been taken vertical (Figure 18) for comparison with symmetric growth. We will use a horizontal orientation in the later analysis. Mechanical factors could dictate other orientations, such as the one shown in Figure 20. In this configuration, point A, which presumably defines the downstream limit of the LSI, is fixed by meniscus stability consideration.[8] The wedge angle, θ, is given by

$$\theta \approx \varepsilon\sigma\,(T_F^4 - T_0^4)/\rho v L \text{ radian} \qquad (27)$$

if heat flux into the LSI from the melt is neglected.[5] If the top-side ambient T_0 is 300°K, this becomes

$$\theta \approx 0.005/v$$

and for pull speeds of the order of 0.1 cm/sec or higher, the wedge angle is less than 3 degrees. Although θ is established by thermal considerations involving the pull speed, the thickness t is not, since

$$t \approx \theta \cdot AB \tag{28}$$

and the length AB is an adjustable parameter based upon the design of the apparatus. The position of B might be fixed, for example, by heating the melt surface to the left of B and allowing it to cool on the right. Equations (27) and (28) show that an indirect tradeoff exists between v and t; given a fixed wedge length AB, t is inversely proportional to v. For the subsequent calculations, this dimension is arbitrarily assumed to be 0.8 cm.

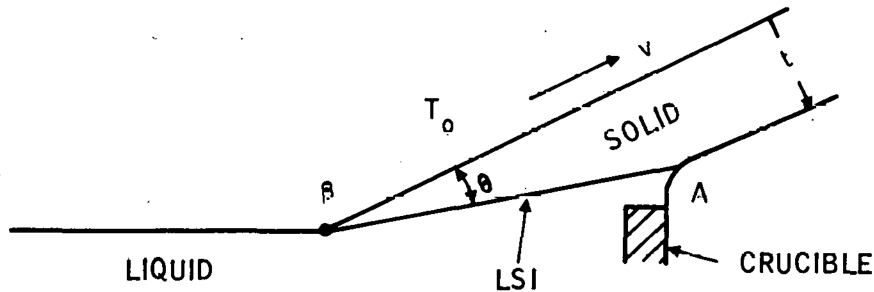

Figure 20. Nonvertical Implementation of Asymmetric Growth

Temperature Profile in the Solidification Region

Subject to a number of assumptions which will be examined, the two-dimensional heat equation yields a nearly linear temperature distribution in the solid portion of the region x = to x = ℓ (see Figure 21):

$$T(x, y) \simeq T_F - \Delta \cdot (x/\ell - y/t) \tag{29}$$

with

$$\Delta \simeq \epsilon\sigma (T_F^4 - T_o^4) \cdot t/k \tag{30}$$

and

$$t/\ell \simeq \theta \simeq \epsilon\sigma (T_F^4 - T_o^4)/\rho v L \tag{31}$$

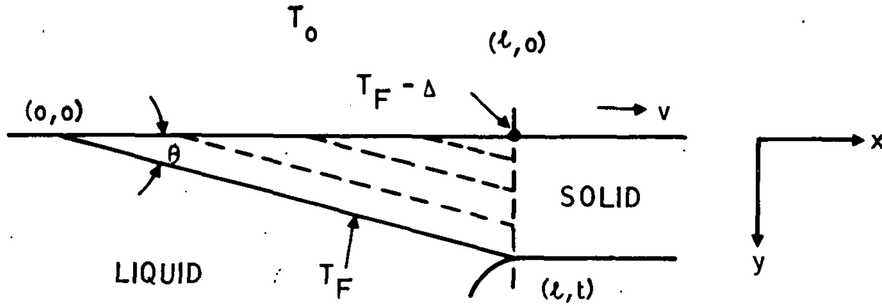

Figure 21. Linear Temperature Distribution in a Wedge-Shaped Solidification Region

The validity of the assumptions rests on their self-consistency, which we will attempt to establish:

1) We assume the LSI is indeed a straight line and an isotherm at temperature T_F.

2) Given (a), the linear temperature distribution obviously satisfies the steady-state heat equation:

$$k(\partial^2 T/\partial x^2 + \partial^2 T/\partial y^2) - \rho c v \, \partial T/\partial x = 0 \tag{32}$$

provided that the $\rho c v$ term can be neglected. Zoutendyk[5] gives the following condition for neglecting the $\rho c v$ term:

$$vt << k/\rho c = 0.097 \tag{33}$$

We will return to this condition.

3) A heat flux emerges from the LSI due to the latent heat of fusion. If there are no temperature gradients in the liquid, this flux is normal to the LSI and of constant density,

$$J = \rho v L \sin \theta \tag{34}$$

because the LSI is a straight line of length $t/\sin \theta$ and the total flux is $\rho v L t$. From Equations (34) and (29) we see that

$$J_x = k\Delta/\ell = \rho v L \sin^2\theta \tag{35}$$

and

$$J_y = k\Delta/t = \rho v L \sin\theta \cos\theta \tag{36}$$

4) The radiated flux density from the surface $y = 0$ is approximately constant, provided that Δ is small, and equal to $\epsilon\sigma(T_F^4 - T_o^4)$. Equating this to the vertical component J_y in (3) gives

$$\Delta \simeq \epsilon\sigma(T_F^4 - T_o^4) \cdot t/k$$

which establishes Equation (30) and confirms that Δ is small ($\Delta = 4.9$ deg if $t = 0.1$ cm).

5) Combining Equations (30) and (36) also give

$$\sin\theta \cos\theta \approx \theta \approx \epsilon\sigma(T_F^4 - T_o^4)/\rho v L$$

which establishes Equation (31). Finally, since $\theta \simeq t/\ell$, Equation (31) may be rewritten

$$vt \simeq \epsilon\sigma(T_F^4 - T_o^4) \cdot \ell/\rho L$$

or $vt \simeq 0.005$ if $\ell \simeq 1$ cm. (It has been already noted that ℓ is somewhat arbitrary.) Since $0.005 << 0.97$, the condition (24) for neglecting the $\rho c v$ term is satisfied.

Matching the Temperature Distribution to the Downstream Region

As observed previously, the component of latent heat carried downstream is much smaller in asymmetric than in symmetric growth. In fact, since $J_x = \rho v L \sin^2\theta \simeq [\epsilon\sigma(T_F^4 - T_o^4)]^2/\rho v L$ from Equations (35) and (31), the conservation principle for the wedge model becomes

$$[\epsilon\sigma(T_F^4 - T_o^4)]^2/\rho v L k = q|_T \sim T_F \tag{37}$$

For a cooling environment of 300°K along the whole silicon ribbon, q was found to be in the 10^2 to 10^4 deg/cm range (Figure 19), whereas the left-hand side of Equation (37) is much smaller (e.g., about 5 deg/cm for $v = 0.1$ cm/sec). It is obvious that the cold downstream environment is not compatible with the wedge model. We will see in more detail later (Figure 26) what happens when we try to force the cold downstream environment on the wedge model.

It is not so obvious that the cold environment precludes any kind of asymmetric growth. It is conceivable that some kind of curved LSI is possible with a portion of it nearly parallel to the surface, for higher throughput, and another portion at a large inclination to the surface in order to match the high q. We have not succeeded in constructing such a curve by any analytical method, and we also doubt that this type of geometry would be stable in practice.

The approach taken here is an attempt to stabilize the wedge pattern by extending the linear distribution for some distance into the downstream region. This will automatically satisfy continuity of not only $\partial T/\partial x$ but $\partial T/\partial y$ as well. It is assumed that afterheaters can be constructed to provide an arbitrary distribution, $T_A(x)$, of effective ambient temperature on the meniscus side of the ribbon. The other side will remain exposed to the cold ambient. A restriction on this approach is that $T_A(x)$ (i.e., the design of the afterheaters) must depend on v and t. A change in either of these parameters would force a redesign of the afterheaters. The required $T_A(x)$ is estimated using the one-dimensional heat equation, Equation (25) and then "verified" by applying it to a computer program which (numerically) solves the two-dimensional heat equation for the entire silicon ribbon. The method is demonstrated for the particular case ℓ = 0.8 cm, v = 0.1 cm/sec, and t = 0.04 cm.

To begin, let $F(T, T_A)$ in Equation (25) be written

$$F[T, T_A(T)] = f(T, 300) + f[T, T_A(T)] \quad (38)$$

where $f(T, U) = \epsilon\sigma(T^4 - U^4)$ and hence $F(T, 300) = 2f(T, 300) = 2\epsilon\sigma(T^4 - 300^4)$. The procedure will be to find a $T_A(T)$ to suit our purposes and then convert to $T_A(x)$ using

$$x = \ell + \int_{T_F}^{T} -dT/q(T) \quad (39)$$

where q is obtained from Equation (25) with $T_A = T_A(x)$. Let $q_o(T)$ be the integral of Equation (25), with T_A = 300°K. This is plotted in Figure 22 over the range T ~ 1685°K to T = 1200°K. For the desired distribution q(T), let the linear temperature range (constant $q = \Delta/\ell$) be extended to $x = 1.2\ell$ = 0.96 cm, and let T_1 and T_2 denote the half-thickness temperatures at $x = \ell$ and $x = 1.2\ell$, as in Figure 23. The values of T_1 and T_2 are indicated in Figure 22. Next, let q(T) increase as the temperature decreases from T_2 and join it smoothly to $q_o(T)$ at some T_3, as in Figure 21. "Smoothly" means that $q = q_o$ and $dq/dT = dq_o/dT$ at $T = T_3$.

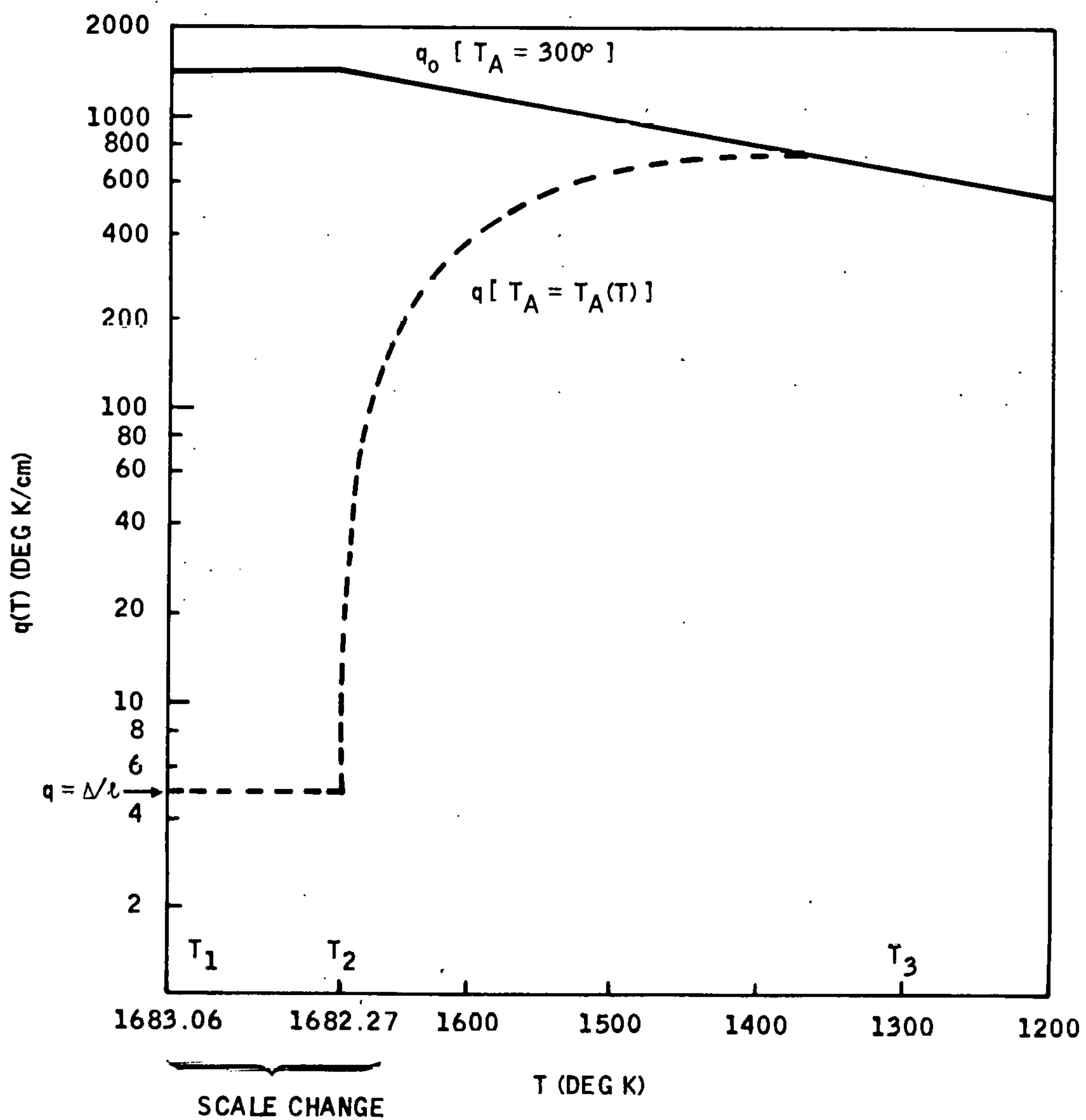

Figure 22. Original (q_o) and Afterheater-Modified (q) Temperature Gradients for the Case v = 0.1 cm/sec, t = 0.04 cm

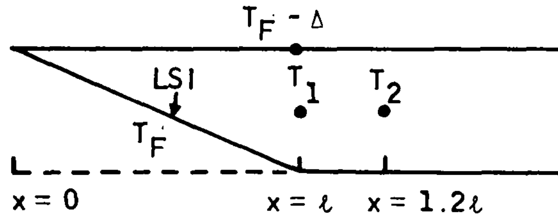

Figure 23. Linear Temperature Distribution to be Extended to $x = 1.2\,\ell$. Then $T_1 = T_F - \Delta/2$ and $T_2 = T_1 - 0.2\Delta$.

Some observations may be inferred from the approach as outlined so far. It will be noted that q and q_o satisfy

$$t(k\, q\, dq/dT + \rho cv\, q) = F[T, T_A(T)]$$

and

$$t(k\, q_o\, dq_o/dT + \rho cv\, q_o) = F(T, 300)$$

Inspection of Figure 22 reveals that $q \le q_o$ and $q dq/dT \le q_o dq_o/dT$. It follows that $F(T, T_A(T)) \le F(T, 300)$, and, therefore, $T_A(T) \ge 300$. In other words, $T_A(T)$ is realisable with heaters. Second, since both q, q_o and their derivatives match at $T = T_3$, the value of $T_A(T)$ falls to 300° at $T = T_3$ and remains constant at lower ribbon temperatures. Finally, to the same approximations that were discussed earlier, continuity of both dT/dy and dT/dx is assured at $x = \ell$. That is, the linear temperature distribution is extended past $x = \ell$: (a) Since dT/dx is constant by design throughout the extension, dT/dy is also constant throughout the extension because $d^2T/dx^2 + d^2T/dy^2 = 0$ (neglecting the ρcv term). (b) Because the ambient seen by the ribbon surface opposite the meniscus is 300°K, it follows that

$$dT/dy \simeq 1/k\, f(T_F, 300)$$

throughout the extension, as it is also in the wedge region. This is the primary rationale for placing the afterheaters on the meniscus side.

A simple function having the required properties is

$$q(T) = \Delta/\ell + a_1(T_2 - T) + a_2(T_2 - T)^2 \text{ where } T_2 \ge T \ge T_3 \tag{40}$$

with a_1 and a_2 chosen so that $q(T_3) = q_o(T_3)$ and $q'(T_3) = q_o'(T_3)$. If $T_3 = 1300°K$, these are $q(T_3) = 672.17$ and $q'(T_3) = 1027.46$, and the coefficients are found to be $a_1 = 5.0197$ and $a_2 = -0.0085649$. Now $T_A(T)$ is easily determined algebraically from Equation (25) over the range $T_1 \geq T \geq T_2$ using $q = \Delta/\ell$ and $q' = 0$, and over the range $T_2 \geq T \geq T_3$ using q and q′ from Equation (40). Then $T_A(x)$ may be found by integrating as in Equation (39) to obtain the relation between x and T. (This temperature distribution appears in Figure 25.)

Two-Dimensional Verification

The two-dimensional steady-state heat equation, Equation (32) was solved numerically on a 7 x 300 grid representing a rectangular region t = 0.04 cm wide and about 2.4 cm long. The first 0.8 cm (~100 grid points) corresponds to the wedge portion, the next 0.16 cm (20 grid points) represents the linear extension region, $T_1 \geq T \geq T_2$, and the remainder covers the rest of the afterheater distribution, including a very short final portion (~0.04 cm) where $T_A = 300°K$. Boundary conditions were set up as indicated in Figure 24. Temperatures were specified on segments 1, 2, and 5, whereas derivative conditions were used on segments 3 and 4 corresponding to the nonlinear radiation law. An approximately linear temperature distribution was set up in the wedge region by treating the liquid as an extension of the solid. The temperature on the edge segments 1 and 2 was set to increase linearly from T_F at the LSI corners to $T_F + \Delta$ at (o, t).

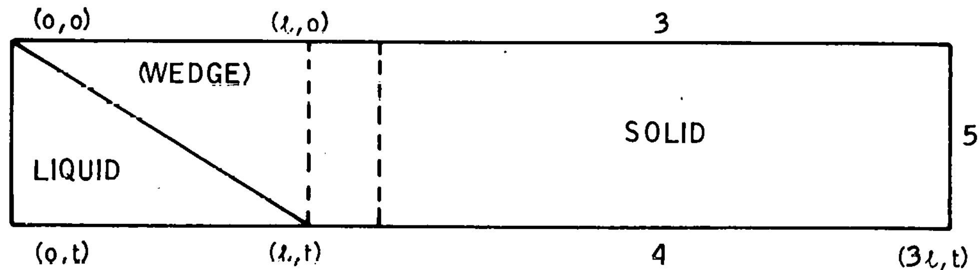

Figure 24. Boundary Conditions for Numerical Integration of Equation (32). Segment 1: $T = T_F + (y/t)\Delta$ Segment 2: $T = (T_F + \Delta) - (x/\ell)\Delta$. Segment 3: $|\partial T/\partial y| = (1/k)\, f\,(T, 300)$. Segment 4: $|\partial T/\partial y| = (1/k)\, f\,[T, T_A(x)]$. Segment 5: $T = 1275$.

The 2100-point system was solved by means of a successive over-relaxation method. The main features of the calculated temperature distribution are plotted in Figure 25 along with the effective ambient, $T_A(x)$. The partials $\partial T/\partial x$ and $\partial T/\partial y$ are of particular interest and are seen to remain essentially constant through the solidification region, ending at the point marked with an arrow. In other words, the linear profile remains intact throughout this region. The required T_A is approximately constant at just over 2000°K to a distance of 1 cm from the LSI-meniscus juncture and then falls rapidly to 300°K over the next 0.55 cm.

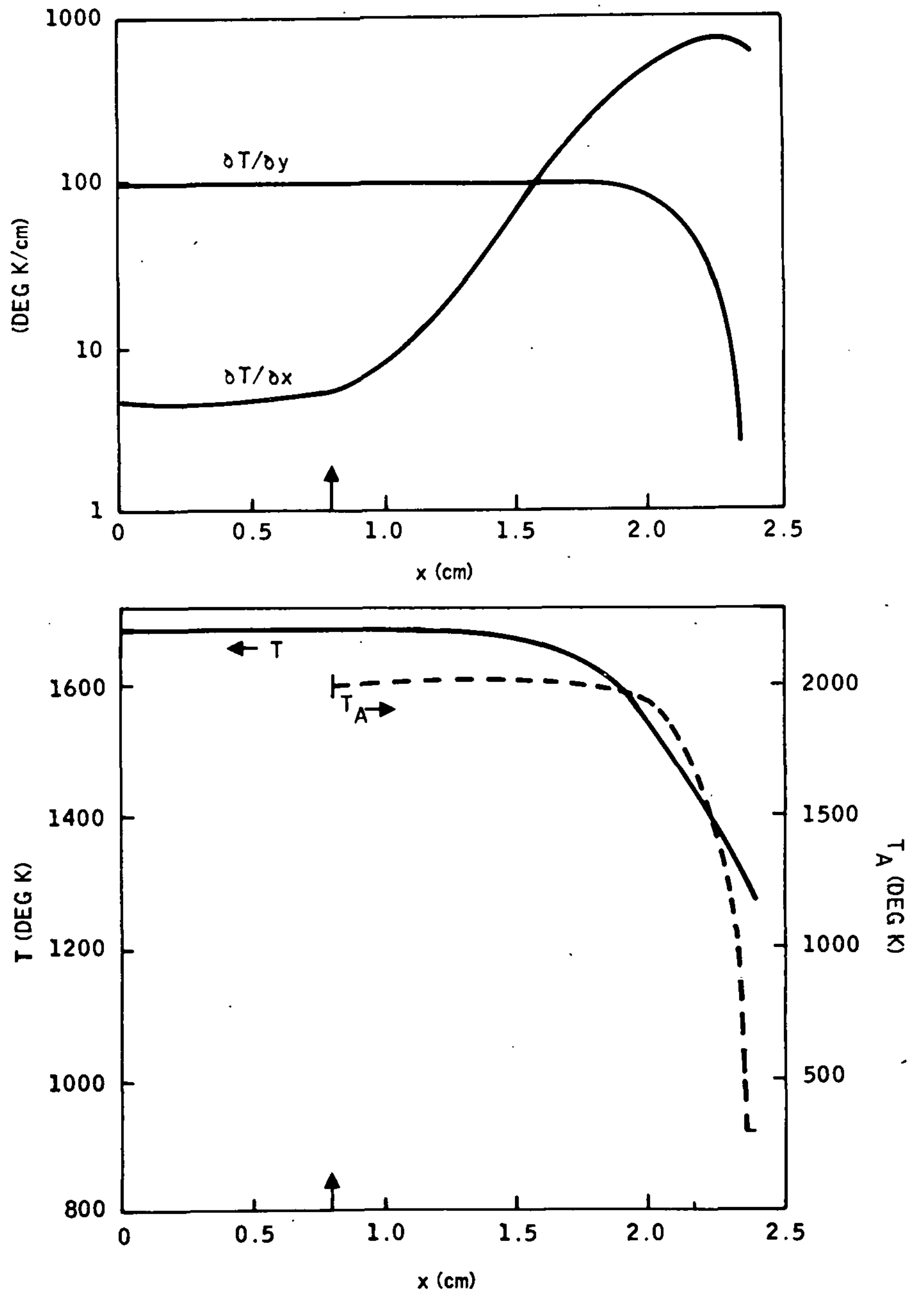

Figure 25. Two-Dimensional Temperature Distribution in Silicon Ribbon Drawn Through the Heated Environment, $T_A(x)$ (dashed curve). T and the partials, $\partial T/\partial x$ and $\partial T/\partial y$, are averaged over the width of the ribbon. A well-established linear temperature distribution is indicated by the near constancy of $\partial T/\partial /x$ and $\partial T/\partial y$ up to the end of the wedge (marked with an arrow).

For comparison, Equation (32) was solved with $T_A(x)$ set equal to 300°K, corresponding to the omission of afterheaters. The boundary conditions on segments 1, 2, and 3 were the same as given in the caption for Figure 24 but on segment 4, $|\partial T/\partial y| = (1/k)\, f(T, 300)$. The results are plotted in Figure 26. Note that the rapid downstream cooling causes drastic variations in both $\partial T/\partial x$ and $\partial T/\partial y$ near the LSI-meniscus juncture. It is clear that the linear temperature distribution is completely destroyed.

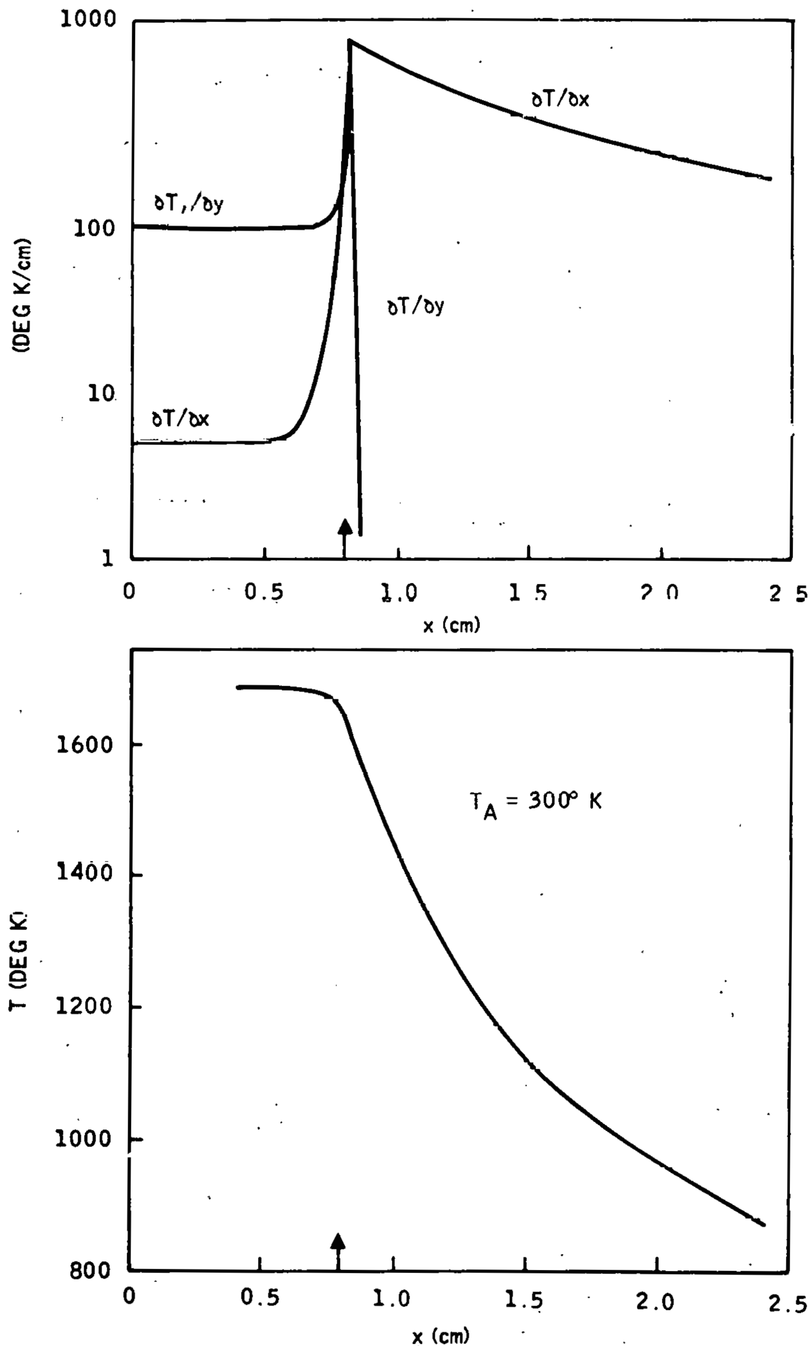

Figure 26. Two-Dimensional Temperature Distribution in Silicon Ribbon With No Heated Environment. The linear temperature distribution is totally destroyed, indicating that a wedge-shaped solidification zone is not possible in a cold environment.

CONCLUSIONS AND RECOMMENDATIONS

CONCLUSIONS

From the work performed during the quarter, we conclude that:

- Smooth 125 μm layers can be produced in the experimental dip coater at pull speeds of 0.15 cm/sec.
- An active afterheater must be provided for the experimental dip coater to minimize thermal shock to the ceramic substrate.
- A leak in a valve in the argon line of the production dip coater was causing unwanted SiC formation in the melt.
- Unidirectional solidification with large grain size occurs even at a pull speed of 0.2 cm/sec.
- Angle SCIM coating can provide the meniscus stability necessary for continuous coating operation.
- The optimum base doping concentration for relativelv thick SOC cells is 1×10^{16}/cc.
- "Good" solar cells (> 9 percent cell efficiency) can be processed on 120μm-thick SOC material.
- Thin SOC cells will not be unduly affected by increased series resistance (≈0.5 percent cell efficiency.)
- Initial SCIM material has a minority carrier diffusion length of $L_n = 34 \pm 3$μm.
- LBIC measurements indicate L_n decreases as the dip number increases for dip coated samples (L_n decreases by ≈ a factor of 2 after 23 dips).
- Good agreement between theory and experiment (LBIC) with respect to loss of J_{sc} out to grain boundaries can be obtained.
- Growth modeling activities indicate the asymmetric growth mode may offer an improved thickness/velocity relationship.

RECOMMENDATIONS

Recent experimental results indicate good cell performance can be obtained on thinner material (faster growth speed). Also, we have found that an N_D value of 1×10^{16}/cc in the base region provides improved cell performance. Therefore, we recommend the "standard" pull speed be increased to 0.07 to 0.08 cm/sec and the standard base doping concentration be reduced to 1×10^{16}/cc.

PROJECTION OF FUTURE ACTIVITIES

Future activities are projected as follows:

- An active afterheater will be added to our experimental dip coater to minimize thermal shock to the substrate.
- Coating experiments with convective cooling will be carried out at 0.2 to 0.3 cm/sec in the experimental dip coater.
- Thin material (100 to 125 μm) will be fabricated in the production dip coater for SOC cell fabrication.
- The transverse thermal gradient along the trough in the SCIM coater will be eliminated.
- The effect of coating angle, coating speed, substrate and meniscus temperature on SCIM-coated layer quality will be investigated.
- Thin (50 to 100 μm) SOC cells will be fabricated and evaluated.
- Photodiodes/solar cells will be fabricated on SCIM-coated material.
- LBIC measurements will continue on selected dip-coated and SCIM-coated material
- Growth modeling activities will be directed toward supported asymmetric growth.

NEW TECHNOLOGY

There were no reportable "new technology" items uncovered during this reporting period.

PROGRAM STATUS UPDATE

Updated versions of the Program Plan, Program Labor Summary, and Program Cost Summary are presented in Figures 27, 28, and 29, respectively.

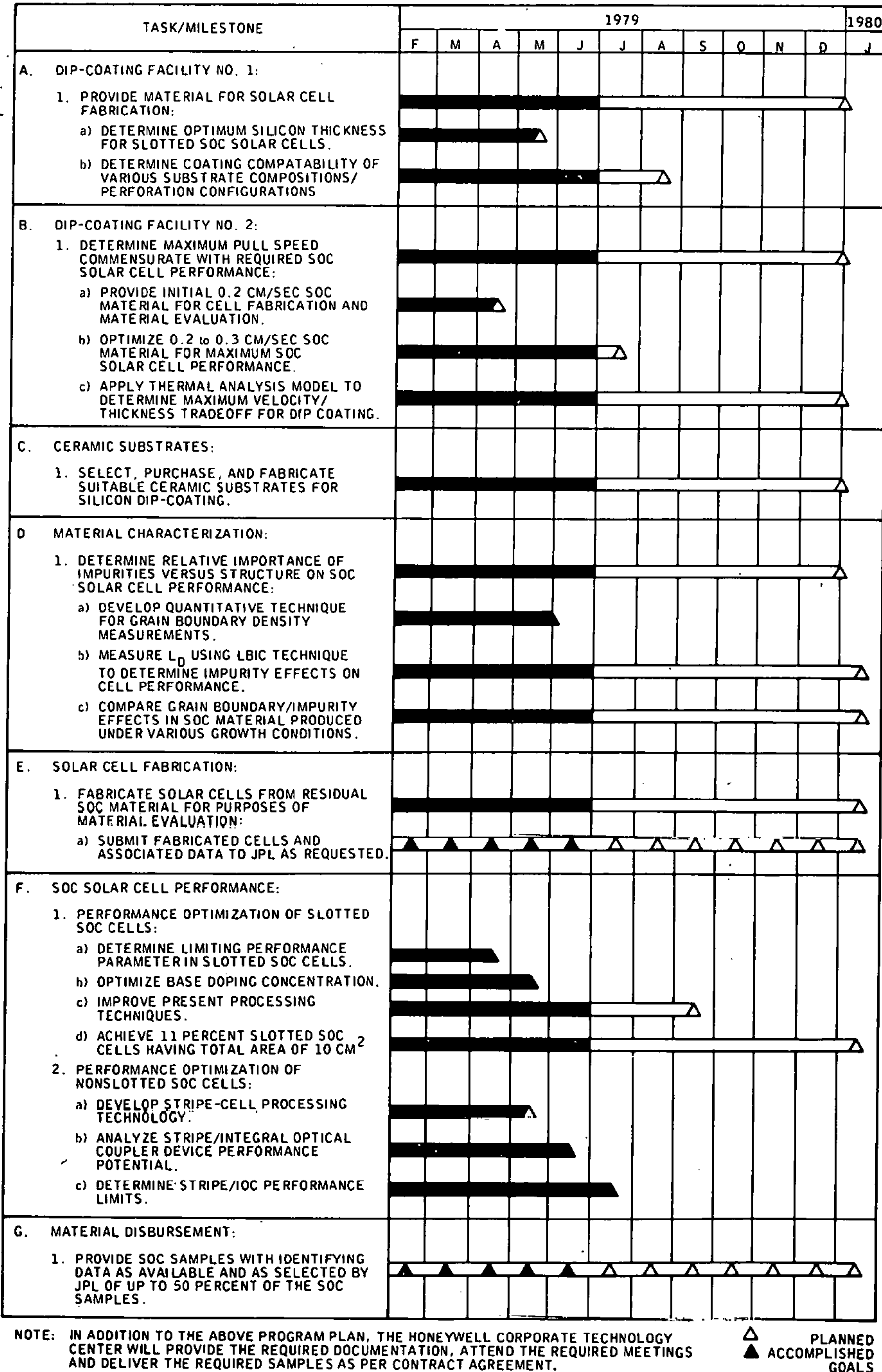

Figure 27. Updated Program Plan

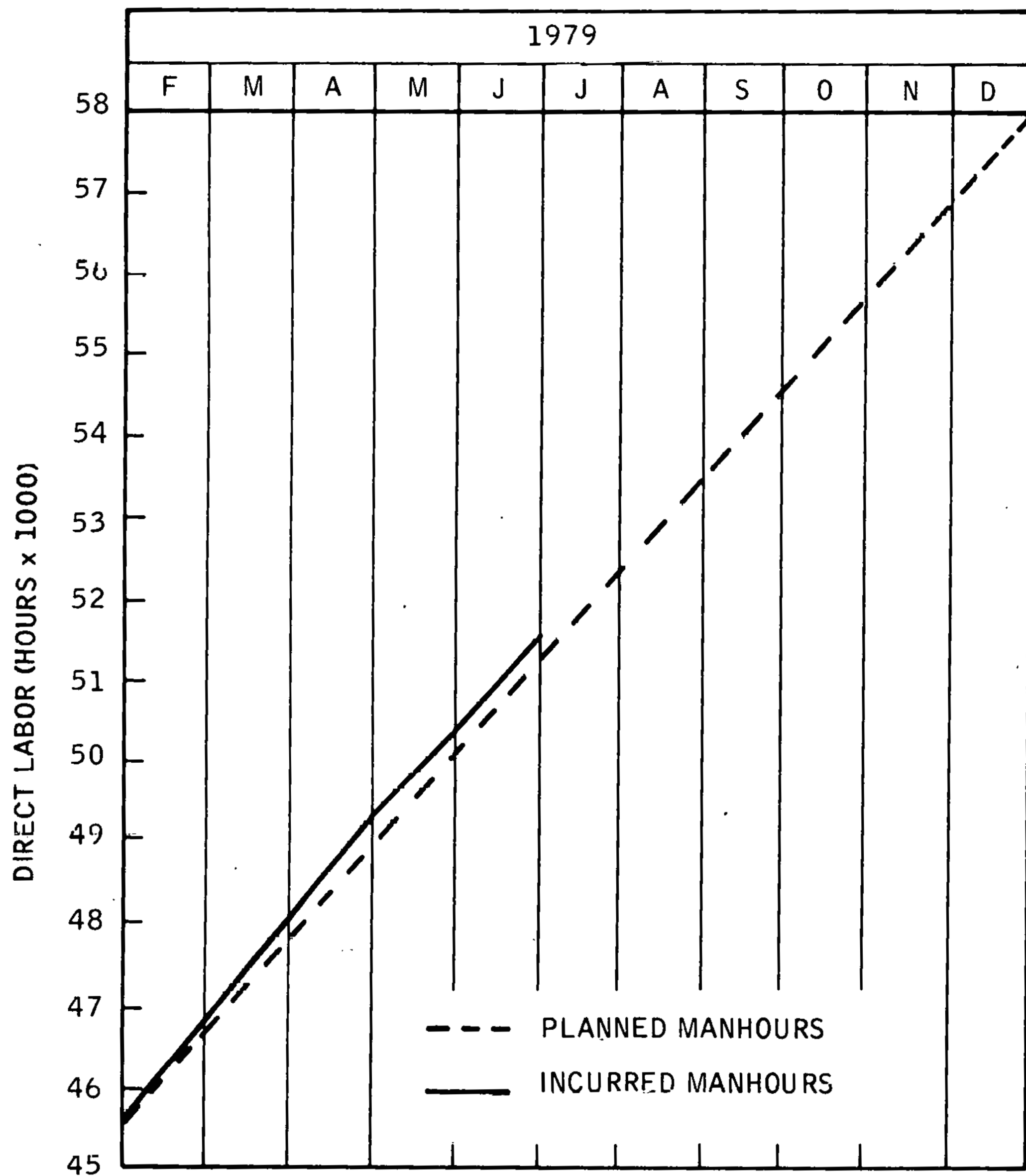

Figure 28. Updated Program Labor Summary

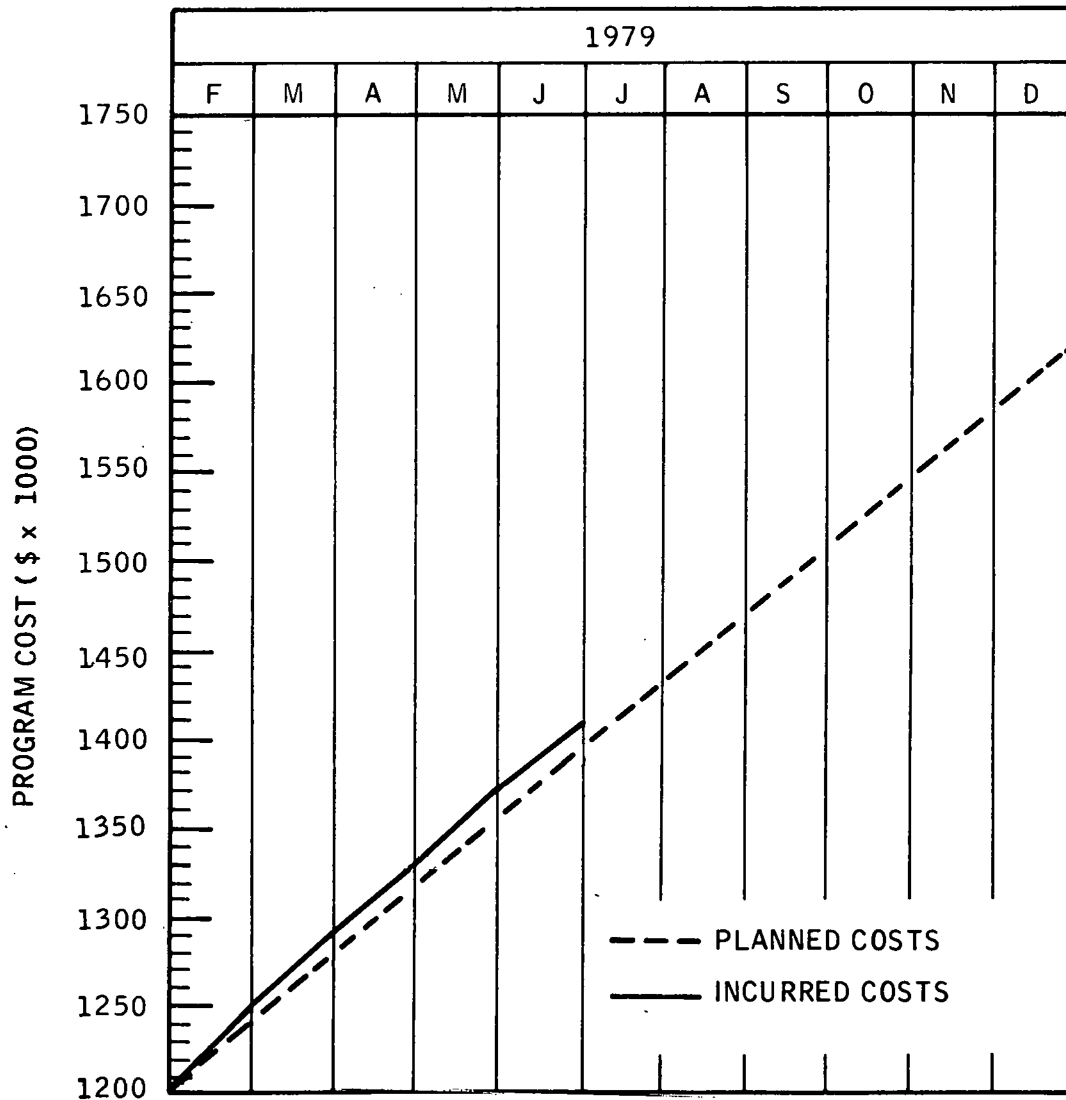

Figure 29. Updated Program Cost Summary

REFERENCES

1. F. Schmid, C. P. Khatlak, T. G. Diggs, Jr. and L. Kaufmann, J. Electrochemical Soc. 126, 935 (June, 1979).

2. W. van Roosbroeck, "Injected Current Carrier Transport in a Semi-Infinite Semiconductor and the Determination of Lifetimes, and Surface Recombination Velocities," J. Appl. Phys. 26, 380-391 (1955).

3. C. Hu and C. Drowley, "Determination of Diffusion Length and Surface Recombination Velocity by Light Excitation," Solid State Elec. 21, 965-968 (1978).

4. O. V. Roos, "Analysis of an Electron Beam with a Solar Cell - I," Solid State Elec. 21, 1063-1067 (1978).

5. J. Zoutendyk, "Theoretical Analysis of Heat Flow in Horizontal Ribbon Growth From a Melt," J. Appl. Phys. 49(7), July, 1978, pp. 3927-3921.

6. J. D. Zook and S. B. Schuldt, "Analysis of Conditions for High-Speed Growth of Silicon," to be published in J. Crystal Growth.

7. Fourth-order Runge-Kutta method.

8. C. A. Rhodes, M. M. Sarraf, and C. H. Liu, "Investigation of the Meniscus Stability in Horizontal Crystal Ribbon Growth," to be published in J. Crystal Growth.

☆U.S. GOVERNMENT PRINTING OFFICE: 1979-640-258-1599